

AD-A273 591

Reproduced From
Best Available Copy

Present Report
AIC-197

ASR-9 Microburst Detection Algorithm

93-29985

O. J. Newell
J. A. Cullen

12 October 1993

Lincoln Laboratory

MASSACHUSETTS INSTITUTE OF TECHNOLOGY

LINCOLN, MASSACHUSETTS



Prepared for the Federal Aviation Administration

Document available to the public through
the National Technical Information Service,
Springfield, Virginia 22161.

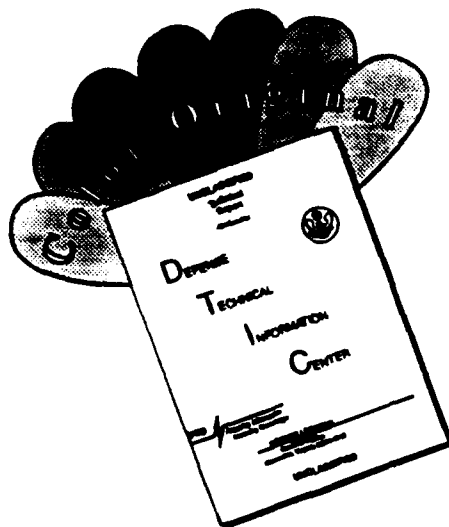
| | |
|---|-------------------------------|
| This document has been approved for public release distribution is unlimited | on approved sale, its d |
|---|-------------------------------|

QR 12 8 06

This document is classified "Secret" under the sponsorship of the Department of Defense operations in the interest of national security. The United States Government assumes no liability for its contents or use thereof.

Reproduced From
Best Available Copy

DISCLAIMER NOTICE



THIS DOCUMENT IS BEST QUALITY AVAILABLE. THE COPY FURNISHED TO DTIC CONTAINED A SIGNIFICANT NUMBER OF COLOR PAGES WHICH DO NOT REPRODUCE LEGIBLY ON BLACK AND WHITE MICROFICHE.

| | | | |
|--|--|---|-----------|
| 1. Report No. ATC-197 | 2. Government Accession No. DOT/FAA/NR-93/2 | 3. Recipient's Catalog No. | |
| 4. Title and Subtitle ASR-9 Microburst Detection Algorithm | | 5. Report Date 22 October 1993 | |
| | | 6. Performing Organization Code | |
| 7. Author(s) Oliver J. Newell and Joseph A. Cullen | | 8. Performing Organization Report No. ATC-197 | |
| 9. Performing Organization Name and Address Lincoln Laboratory, MIT P.O. Box 73 Lexington, MA 02173-9108 | | 10. Work Unit No. (TRAIS) | |
| | | 11. Contract or Grant No. DTFA01-89-Z-02030 | |
| 12. Sponsoring Agency Name and Address Department of Transportation Federal Aviation Administration Systems Research and Development Service Washington, DC 20591 | | 13. Type of Report and Period Covered Project Report | |
| | | 14. Sponsoring Agency Code | |
| 15. Supplementary Notes This report is based on studies performed at Lincoln Laboratory, a center for research operated by Massachusetts Institute of Technology under Air Force Contract F19628-90-C-0002 | | | |
| 16. Abstract The ASR-9 Wind Shear Processor (WSP) is intended as an economical alternative for those airports that have not been slated to receive a Terminal Doppler Weather Radar (TDWR) but have, or will be receiving, an ASR-9 radar. Lincoln Laboratory has developed a prototype ASR-9 WSP system which has been demonstrated during the summer months of the past three years in Orlando, Florida. During the operational test period, microburst and gust front warnings, as well as storm motion indications, were provided to the Air Traffic Control in real time. The ASR-9 Microburst Detection Algorithm (AMDA) is based on the earlier TDWR Microburst Detection Algorithm but has been substantially modified to match better the particular strengths and weaknesses of the ASR-9 rapid-scanning fan-beam radar. The most significant additions include a capability to detect overhead microbursts, a reflectivity processing step used to help detect velocity signatures that have been biased by overhanging precipitation, and a modification to some of the shear segment grouping and thresholding parameters to accommodate better the typical on-air siting of the ASR-9. In addition, the AMDA has been designed to be as efficient as possible to allow it to run at the radar's 4.8 seconds/scan antenna rotation rate on a single-board computer. A detailed description of AMDA, as well as the performance evaluation strategy and results, are presented in this report. | | | |
| 17. Key Words ASR-9 algorithm microburst MIGRA WSP | | 18. Distribution Statement This document is available to the public through the National Technical Information Service, Springfield, VA 22161. | |
| 19. Security Classif. (of this report) Unclassified | 20. Security Classif. (of this page) Unclassified | 21. No. of Pages 71 | 22. Price |

ABSTRACT

The ASR-9 Wind Shear Processor (WSP) is intended as an economical alternative for those airports that have not been slated to receive a Terminal Doppler Weather Radar (TDWR), but have, or will be receiving, an ASR-9 radar. Lincoln Laboratory has developed a prototype ASR-9 WSP system which has been demonstrated during the summer months of the past 3 years in Orlando, Florida. During the operational test period, microburst and gust-front warnings, as well as storm motion indications, were provided to the Air Traffic Control Tower in real-time.

The ASR-9 Microburst Detection Algorithm (AMDA) is based on the earlier TDWR Microburst Detection Algorithm, but has been substantially modified to better match the particular strengths and weaknesses of the ASR-9 rapid-scanning fan-beam radar. The most significant additions include a capability to detect overhead microbursts, a reflectivity processing step used to help detect velocity signatures that have been biased by overhanging precipitation, and a modification to some of the shear segment grouping and thresholding parameters to make them a function of range. This is necessary to better accommodate the ASR-9. In addition, AMDA has been designed to be as efficient as possible to allow it to run at the radar's 4.8 seconds/scan antenna rotation rate on a single board computer. A detailed description of AMDA, as well as the performance evaluation strategy and results, are presented in this report.

| | |
|--------------------|--|
| Accession For | |
| NTIS CRA&I | <input checked="checked" type="checkbox"/> |
| DTIC TAB | <input type="checkbox"/> |
| Unannounced | <input type="checkbox"/> |
| Justification | |
| By | |
| Distribution/ | |
| Availability Codes | |
| Dist | Avail and/or Special |
| A-1 | |

DTIC QUALITY INSPECTED 3

ACKNOWLEDGMENTS

This work benefited from contributions by a number of people. Mark Weber supplied the signal processing and spatial smoothing algorithms, while Terri Noyes contributed to the shear segment temporal smoothing portion of the algorithm. Jim Pieronek designed the prototype WSP, as well as the IQ data collection system. Bill Moser wrote much of the software used to collect and analyze the early IQ data. The site personnel, Wes Johnston, Craig McFarland, and Jay Laseman, spent many long nights collecting data and have provided many insights into the microburst detection process.

TABLE OF CONTENTS

| Section | Page |
|--|-------------|
| Abstract | iii |
| Acknowledgments | v |
| List of Illustrations | ix |
| List of Tables | xi |
| List of Equations | xi |
| 1. INTRODUCTION | 1 |
| 2. ASR-9 Microburst Signature Characteristics | 3 |
| 2.1 One-Dimensional Divergence Signatures | 3 |
| 2.2 Two-Dimensional Divergence Signatures | 5 |
| 2.3 Microburst Detection Requirements | 7 |
| 3. WIND SHEAR PROCESSOR SYSTEM OVERVIEW | 9 |
| 4. ASR-9 MICROBURST DETECTION ALGORITHM | 11 |
| 4.1 Overview | 11 |
| 4.2 Scan Buffer | 12 |
| 4.3 Segment Detection | 16 |
| 4.3.1 Detect Beginning of Segment | 16 |
| 4.3.2 Search for End of Segment | 16 |
| 4.3.3 Segment Thresholding | 20 |
| 4.4 Segment Temporal Smoothing | 21 |
| 4.5 Segment Association | 22 |
| 4.6 Reflectivity Thresholding | 23 |
| 4.7 Segment Density Thresholding | 24 |
| 4.8 Cluster Shear Determination | 27 |
| 4.9 Area Thresholding | 28 |
| 4.10 Cluster Temporal Smoothing | 30 |
| 4.11 Shape Algorithm and Final Output | 32 |
| 5. MICROBURST ALGORITHM PERFORMANCE EVALUATION | 35 |
| 5.1 Evaluation Strategy and Results | 35 |
| 5.2 Investigation of Algorithm Failures | 37 |

TABLE OF CONTENTS (CONTINUED)

| <u>Section</u> | <u>Page</u> |
|---|--------------------|
| 6. ONGOING ALGORITHM DEVELOPMENT | 51 |
| 6.1 AMDA Enhancements | 51 |
| 6.2 Alternative Algorithm Approaches | 52 |
| 6.2.1 AMDA Development History | 52 |
| 6.2.2 Motivation for Alternative Algorithms | 52 |
| 7. SUMMARY | 55 |
| REFERENCES | 57 |
| APPENDIX A. AMDA PARAMETERS | 59 |

LIST OF ILLUSTRATIONS

| Figure | Page |
|--|------|
| 1. Microburst Viewed by an ASR-9 Radar | 3 |
| 2. Microburst Shear Signature Variations | 4 |
| 3. Microburst Segment Field Variations | 6 |
| 4. ASR-9 Wind Shear Processor | 9 |
| 5. Microburst Detection Algorithm Block Diagram | 11 |
| 6. Example of Classical Microburst Signature | 13 |
| 7. Coordinate System Transformation | 15 |
| 8. Detection of an Overhead Microburst Event | 17 |
| 9. Segment Detection Example | 19 |
| 10. Probability Distribution of Parameter <i>seg_age</i> | 21 |
| 11. Association Criteria Range Dependence | 23 |
| 12. Reflectivity Thresholding of Shear Segments | 24 |
| 13. Reflectivity Thresholding Successfully Eliminating a False Alarm on the Fringe of a Storm Cell | 25 |
| 14. Typical Segment Density Distributions and Associated Clustering Decisions | 27 |
| 15. Shear Magnitude Outlier Rejection | 28 |
| 16. Probability of False Alarm vs. Shear Magnitude | 29 |
| 17. Detected Microburst Area vs. Range | 29 |
| 18. AMDA Area Thresholding | 31 |
| 19. Geographical Situation Display | 33 |
| 20. False Alarm at 7 km, 120 Degrees from ASR due to Elevated Reflectivity Core | 39 |
| 21. Synthesized RHI through Location of False Alarm in Figure 20 | 41 |
| 22. ASR-9 Microburst Detection Algorithm's Use of Velocity Estimates in Areas of Low Signal Return Caused 20 m/s False Alarm | 43 |
| 23. Missed Microburst due to Microburst Algorithm Area Thresholding | 45 |
| 24. Apparent False Alarm by the ASR-WSP System due to Microburst Asymmetry | 47 |

LIST OF TABLES

| <u>Table</u> | <u>Page</u> |
|---|--------------------|
| 1. Hit–Miss Scoring Results for 1991 Orlando Test | 36 |
| 2. Hit–Miss Scoring Results for 1992 Orlando Test | 36 |
| 3. Path–Oriented Scoring Results for 1991 Test | 37 |

LIST OF EQUATIONS

| <u>Equation</u> | <u>Page</u> |
|--|--------------------|
| 1. Area Threshold Range and Shear Dependence | 30 |
| 2. Area Threshold Range Dependence | 30 |
| 3. Area Threshold Shear Dependence | 30 |

1. INTRODUCTION

The ASR-9 Wind Shear Processor (WSP) is being developed as an economical alternative to the Terminal Doppler Weather Radar (TDWR) for those airports not slated to receive a TDWR system. Lincoln Laboratory has been sponsored by the FAA to develop a prototype version of the WSP, including both the hardware and the wind shear detection algorithms. Lincoln Laboratory's ASR-9 testbed has been used to collect data in Huntsville, AL (1987-88), Kansas City, KS (1989), and Orlando, FL (1990-92), and these data have been used to develop and validate the wind shear detection algorithms. In addition, during the summer months of 1990, 1991, and 1992, the prototype WSP was used to conduct operational demonstrations, during which microburst and gust-front warnings, as well as storm motion indications, were provided to the Orlando Air Traffic Control Tower in real time.

The ASR-9 Microburst Detection Algorithm (AMDA) is based on the earlier TDWR Microburst Detection Algorithm, but has been modified to be better suited to the strengths and weaknesses of the ASR-9 radar. In particular, the rapid scan rate of the ASR-9 can provide a faster response time to microburst events, while the wide elevation beam of the ASR-9 as compared with the TDWR makes it more difficult to detect shallow microburst outflows, and can sometimes result in erroneous velocity signatures due to winds aloft. The typical on-airport siting of the ASR-9 has also provided some new challenges, such as the detection of overhead microbursts and the detection of events at short range that span a larger azimuthal extent than those detected by an off-airport TDWR. AMDA also contains new logic to address several known deficiencies in the TDWR algorithm. For example, the TDWR algorithm can sometimes detect excessively long shear segments because the "slope" of the shear segment is only being validated in the vicinity of the segment endpoints. AMDA overcomes this problem by utilizing a sliding window to validate the slope along the entire segment length.

This report describes the ASR-9 microburst detection requirements and the processing steps that make up the ASR-9 Microburst Detection Algorithm. Following the algorithm description, a separate chapter describes the performance evaluation process and results. A final section discusses the current status of the algorithm as well as its future development.

2. ASR-9 MICROBURST SIGNATURE CHARACTERISTICS

A microburst is a sudden downward burst of wind which, upon impact with the ground, results in a divergent wind pattern. This situation is depicted in Figure 1. As can be seen from the figure, detecting the low-level wind shear with an ASR-9 radar is made more difficult than in the case of a TDWR by the cosecant-squared elevation beam pattern, which results in low level wind estimates that can be biased by the winds at higher altitudes. To correct for this situation, a "dual-beam" approach is used, whereby the velocity information from the high beam is used to estimate the value of the higher-altitude wind bias, and correct for it [Weber, 1989].

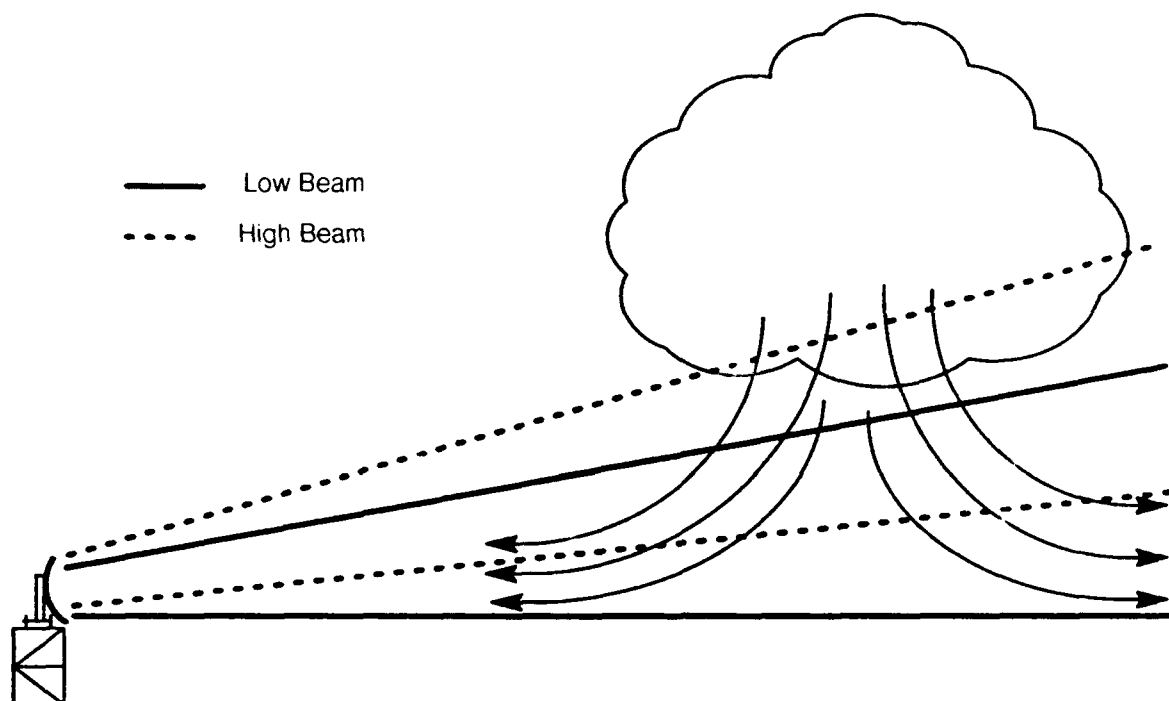


Figure 1. Microburst Viewed by an ASR-9 Radar.

The low level winds originating from a microburst produce a run of radial velocities that are generally increasing with radar range. AMDA detects the microburst using a two-stage approach involving the detection of the microburst signature across range, followed by the grouping of the detected areas across azimuth. The next two sections describe the signatures that are typically encountered in each of the two detection stages, including those that can result in false alarms.

2.1 ONE-DIMENSIONAL DIVERGENCE SIGNATURES

To be considered hazardous, the velocity increase, or "shear," produced by a microburst must exceed 10 m/s over a distance of not more than 4 km. An example of an ideal signature is shown in Figure 2a. The velocity increase is smooth and almost linear, and the endpoints of the shear "segment" are local minima or maxima.

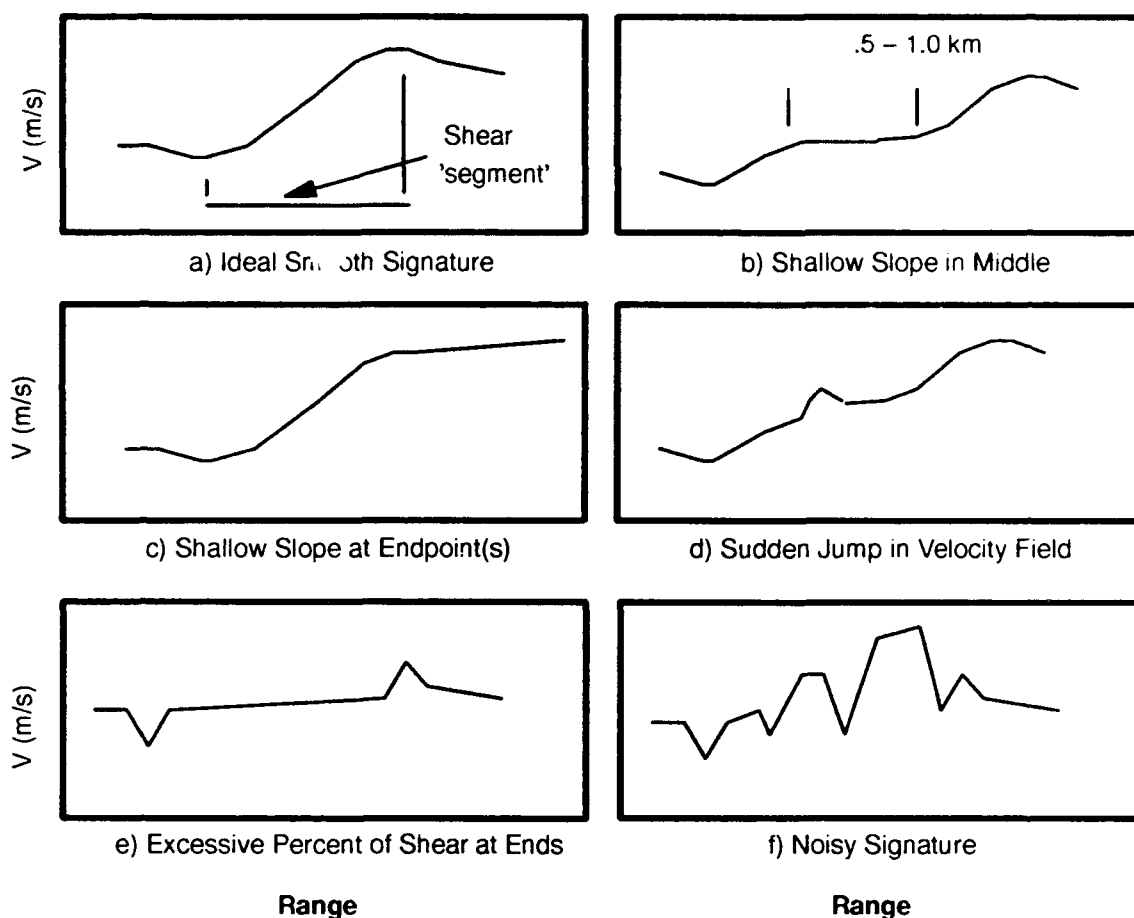


Figure 2. Microburst Shear Signature Variations.

Many signatures very similar to this exist in the actual radar data, but there are several variations that occur quite frequently in wind shear regions, and these also need to be detected. The three most common ones are shown in Figures 2b, 2c, and 2d. Note that the sample segments shown in the figure are representative of velocity radials that have already been spatially smoothed. Figure 2b exhibits a region of extremely shallow or even slightly decreasing slope. This signature occurs most frequently in relatively weak shear segments (< 12 m/s), which are present in both weak microburst events and near the edges of stronger events. Figure 2c is an example of shallow slope near the segment endpoint(s). Because there is no clear cut local maximum or minimum value in these cases, it is sometimes difficult to judge where the starting or ending point of the segment should be placed. The region of shallow slope needs to be trimmed off if detected to avoid an excessively long shear segment.

The signature shown in Figure 2d contains a sudden jump in the velocity field. Even after spatial smoothing, some small discontinuities due to noise or clutter remain and must be handled. The typical jump is 2-3 range gates wide with a velocity difference of about ± 3 m/s at its peak. Regions

with sharper, single-point spikes are also present, but in regions of moderate to high radar reflectivity (25–65 dBz), these are not as prevalent as the smaller jumps.

In regions of low reflectivity (0–15 dBz), the ASR–9 velocity estimate tends to be somewhat noisy, and some of these regions can exhibit an increasing velocity trend that mimics the overall shear and length characteristics of a true shear segment, potentially causing false-alarm problems. Two examples of this kind of behavior are shown in Figures 2e and 2f. The first case (2e) represents a false segment created by noise spikes. The majority of the overall shear in this case can be attributed to the shear at the segment endpoints. The second case (2f) exhibits a generally increasing trend over a suitable range, but the point-to-point velocity differences are far from smooth.

2.2 TWO-DIMENSIONAL DIVERGENCE SIGNATURES

A two-dimensional representation of an idealized microburst, along with the shear segments detected, is shown in Figure 3a. It is cylindrically symmetric and the maximum velocity differential is aligned with the microburst center. Microbursts do sometimes fit this model; however, more often than not they are more irregular in shape and strength. A study performed using data from Denver, CO, Kansas City, KS, and Orlando, FL, determined that the strength asymmetry ratio, the ratio of the maximum velocity differential to the minimum velocity differential when viewing a microburst from all angles, was on average 1.7:1, and can range as high as 4.0:1 [Hallowell, 1993]. In addition, the region of maximum divergence is not always aligned with the center of the microburst, but instead can lie off to one side. Given such variation, a microburst detection algorithm does not have the luxury of requiring microburst events to exhibit a certain two-dimensional velocity profile, but must instead be sensitive to a wide variety of profiles.

The overall size of a microburst also varies significantly over its lifetime, tending to start out small and expand with time. The typical area for a “young” microburst as seen by the ASR–9 is between 1.0–1.5 km², increasing to over 2.0 km² as the microburst matures, or in the case of a line microburst, sometimes exceeding 10 km². The interval between the initial onset of a microburst and the point at which it reaches hazardous intensity can vary from as brief as 30 seconds to upwards of several minutes. Strong microbursts tend to reach hazardous intensities quite rapidly as a direct result of the higher downdraft velocities within the storm cell. In order to detect these events in a timely manner, it is necessary to keep the algorithm latency to a minimum.

Multiple microbursts can exist in the same cloud, and as shown in Figure 3c, they can be closely spaced. In such a case, it is important to resolve them as separate events in order to make an accurate estimate of the microburst’s strength. This is somewhat difficult in practice, because sometimes what begins as a single microburst event can evolve into multiple events, and the point at which to separate the two events is somewhat ill-defined. It is also important to avoid oscillation between a single-event detection and a multiple-event detection, as this can result in inconsistent microburst warnings.

Ground clutter and noise in the velocity field also impact the segment association process. Figure 3d illustrates a case of a true microburst with multiple missing segments due to ground clutter break-

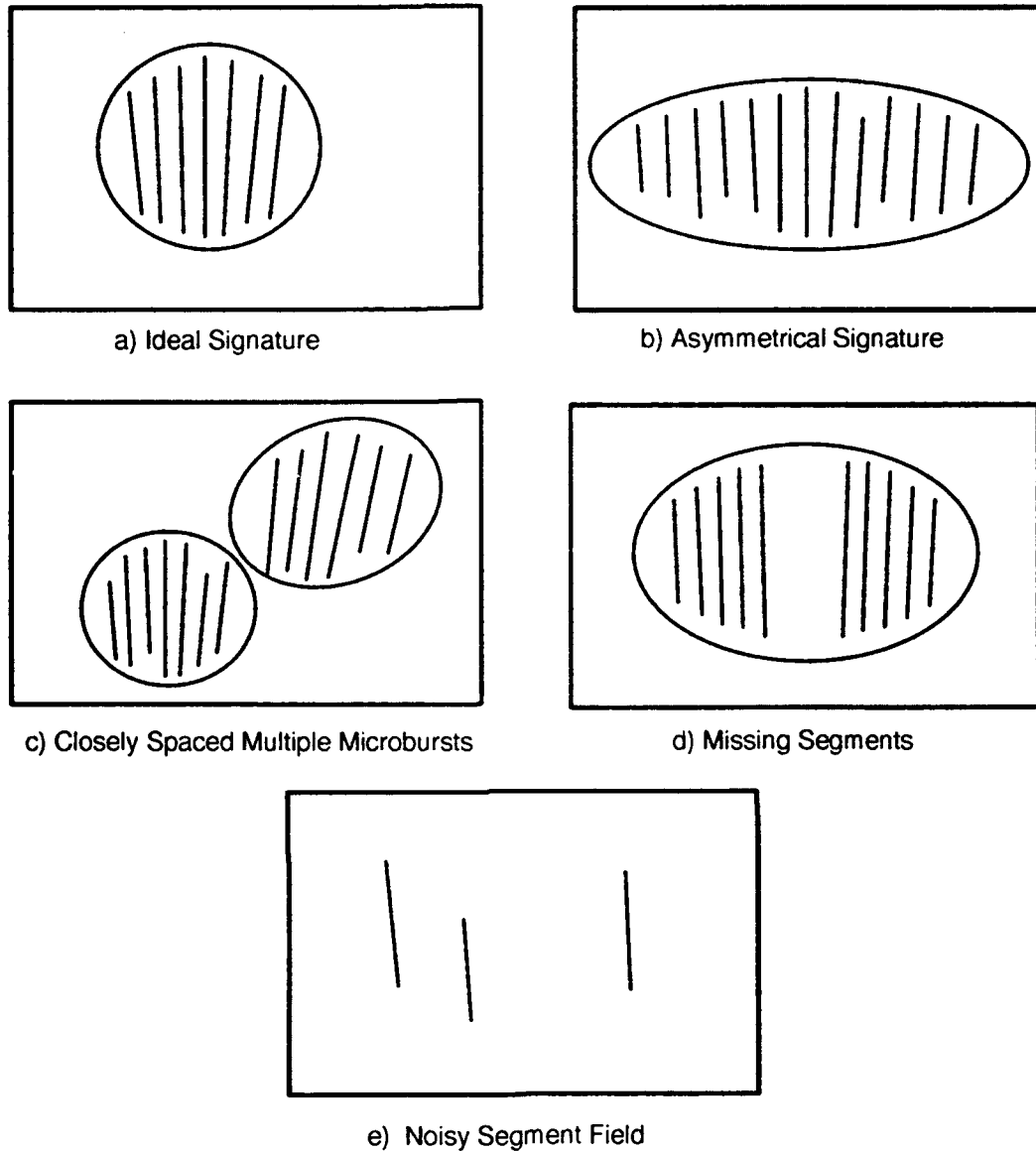


Figure 3. Microburst Segment Field Variations.

through. Figure 3e depicts an area containing a sparse number of segments resulting from noise in the velocity field. To be successful, the detection algorithm must be robust enough to allow a substantial number of missing radials, while at the same time filtering out cases where the overall density of detected segments is low.

2.3 MICROBURST DETECTION REQUIREMENTS

An effective ASR-9 wind shear detection algorithm must be able to reliably identify the variety of microburst radial velocity patterns described above, while at the same time minimizing the number of false signature detections. In addition, the 4.8 seconds/scan update rate of the ASR-9 radar requires an efficient algorithm in order to process the data at real-time rates with the current system configuration. The ASR-9 Microburst Detection Algorithm described in the following sections performs well with respect to all three of these criteria.

3. WIND SHEAR PROCESSOR SYSTEM OVERVIEW

The prototype WSP data processing hardware, as well as the signal processing steps performed prior to the microburst detection algorithm, have both had a significant impact on the design and implementation of AMDA. This section provides a brief description of the processor in order to clarify some of the later discussion.

A block diagram of the prototype WSP is shown in Figure 4. The raw time-series data from the radar A/D converters enter the processor via a custom Lincoln Lab Interface card, are split up into 6 range "rings," and are sent to the six Mercury Computer array processor (MC860 AP) boards. The baseline signal processing sequence used during the Orlando operational tests consisted of:

1. Adaptive clutter filtering [Weber, 1987],
2. Low and high beam reflectivity calculation,
3. Dual-beam velocity calculation [Weber, 1989],
4. Regressive temporal smoothing filter on dual-beam velocity product, and
5. 9-point nearest neighbor median spatial filter (low and high beam reflectivity and dual-beam velocity products).

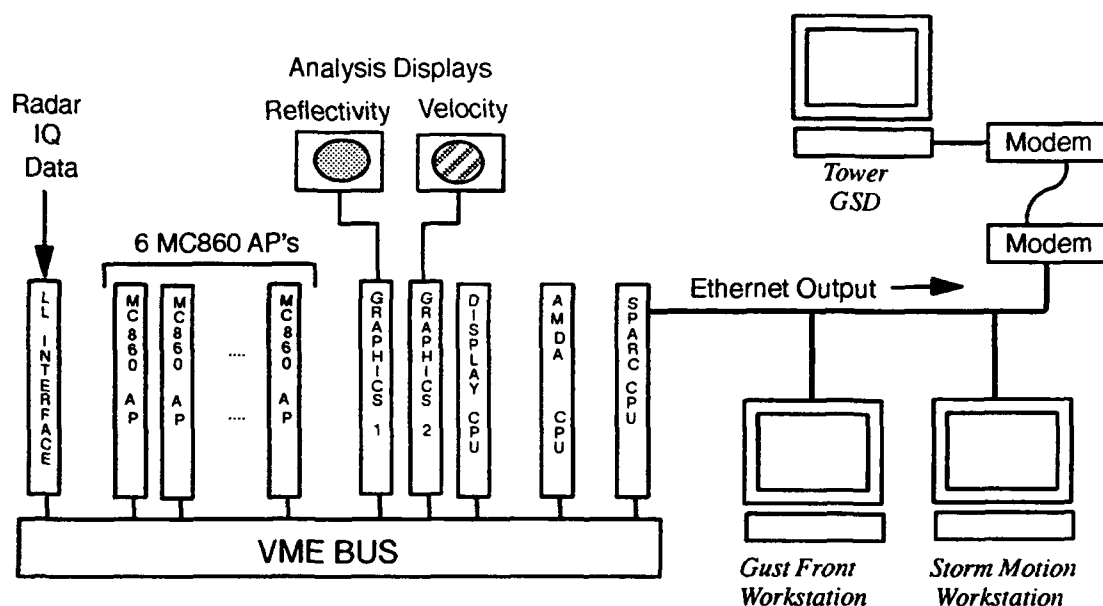


Figure 4. ASR-9 Wind Shear Processor.

Following these operations, the dual-beam velocity and reflectivity data are sent to two Mizar 68030 Single Board Computers (marked "DISPLAY CPU" and "AMDA CPU" above). The display CPU drives two rapid-update analysis displays which provide site personnel with a flexible display

capability at the radar site. The AMDA CPU is used for microburst detection processing, the output of which is sent via Ethernet to the Geographical Situation Displays in the Air Traffic Control Tower. Reflectivity and velocity information are also output using the Ethernet connection. Note that the other WSP algorithms such as gust-front and storm motion are not currently performed in the VME system shown above, but are run on separate SPARC workstations that are connected via Ethernet.

The major points of interest with regard to the design of AMDA are:

- The input reflectivity and velocity data have been spatially and temporally smoothed within the array processor.
- Data are available to the algorithm for every five-second scan, and it is desirable to use all the data for every scan to keep the microburst detection latency to a minimum.
- The algorithm is run on a single 68030 CPU board rated at 5MIPS.

The fact that the input data has been spatially filtered results in radials of velocity data which are generally free from noise and require no additional smoothing in the AMDA processor. This keeps the computational requirements of AMDA to a minimum, allowing data to be processed at real-time rates using a single 68030 CPU board. This is convenient from both the software and hardware standpoints for the prototype WSP.

4. ASR-9 MICROBURST DETECTION ALGORITHM

4.1 OVERVIEW

AMDA is an adaptation of the TDWR Microburst Divergence Outflow Algorithm (MDOA) [Merritt, 1991] that is designed to run efficiently within the prototype WSP's processor. A block diagram of AMDA is shown in Figure 5. The algorithm reads in polar reflectivity and velocity data, scans the radar radials with respect to range for divergent outflow patterns, and groups the detected regions, termed "shear segments," to form microburst events. The first step performed by AMDA is to buffer the data into full scans to allow detection of overhead events in a convenient manner. This is followed by the raw segment detection process that scans the individual radials for microburst signatures. In order to become valid shear segments, any detected signatures are subjected to a variety of segment length and divergent outflow strength tests. The valid raw segments are then temporally smoothed to provide a more consistent output for the subsequent AMDA operations.

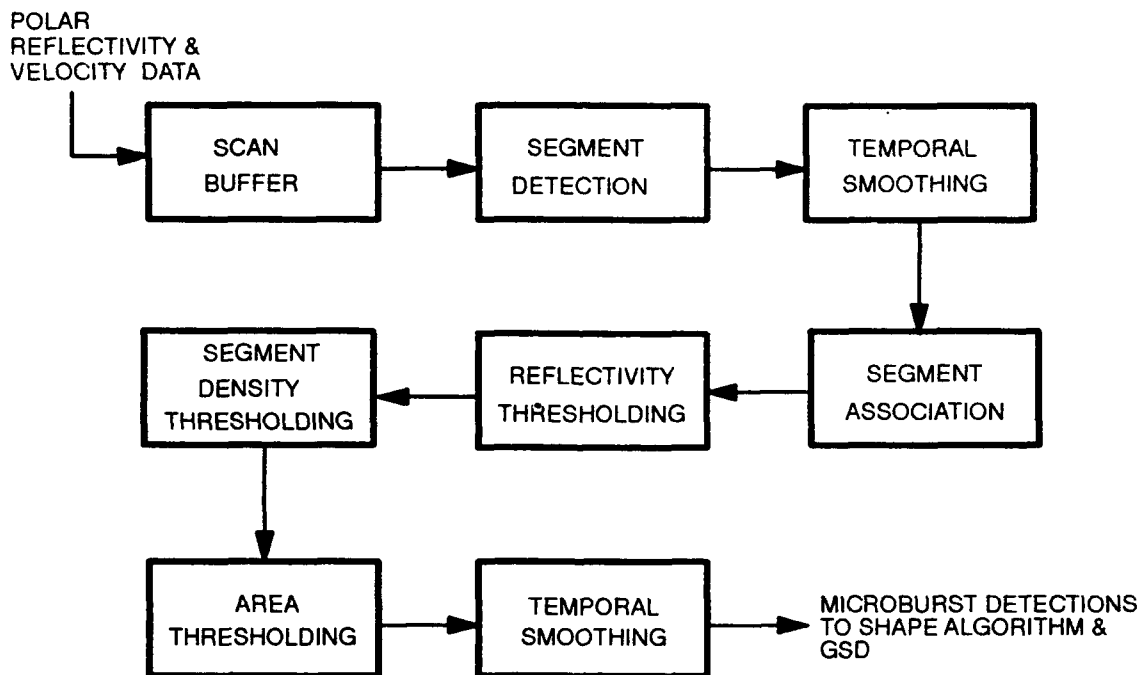


Figure 5. Microburst Detection Algorithm Block Diagram.

The next step, segment association, groups neighboring segments into raw "clusters," requiring that each raw cluster contain a certain minimum number (AMDA parameter) of segments. The raw clusters are then passed to the reflectivity thresholding module, where segments located primarily in regions of low reflectivity (and therefore containing suspect velocity values), are edited out of the cluster. The cluster is again required to possess the minimum number of segments, and clusters that meet the requirement are passed to the segment density thresholding step. This step removes regions

of the cluster where segment density is below a preset minimum, indicative of regions that have been produced by a few spurious segment detections. The modified cluster is again subjected to the minimum segment requirement before being passed to the area thresholding operation. The area thresholding operation rejects any clusters with insufficient area to be considered a true microburst event, and the output clusters are then temporally smoothed to increase the scan-to-scan coherence of the detected microburst events. An example of a "classic" microburst, along with the velocity, reflectivity, and detected shear segment information, is shown in Figure 6. Note that the shape shown in Figure 6 is for the rapid-update analysis displays only. Shear segment data are passed through an additional shape algorithm [Wilson, 1992] to produce the final GSD output.

There are a number of variable site parameters (e.g. length thresholds, time constants, etc.) associated with AMDA. The majority of the parameters in the following discussion will be represented by symbolic names, followed by the current actual value where appropriate (e.g. SEG_MIN_LENGTH (0.96km)). Each of the parameters has been optimized using data from Lincoln Laboratory's ASR-9 testbed.

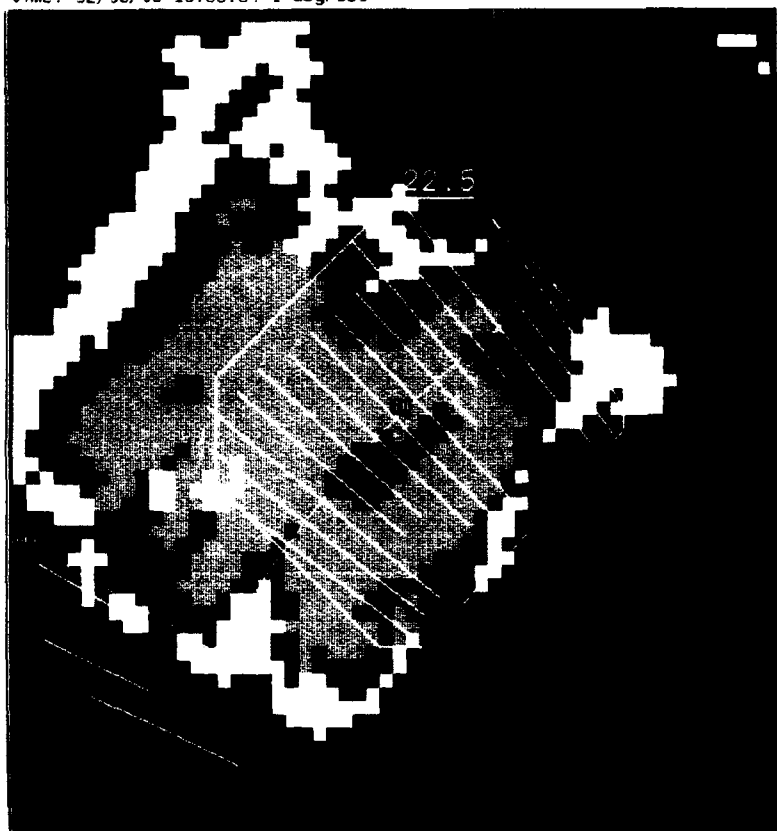
4.2 SCAN BUFFER

The input data stream is in the polar coordinate system, and consists of 256-1.4 deg. radials, or "sectors," per scan. Due to the requirement that the ASR-9 detect overhead microbursts, it is necessary to buffer one scan's worth of data prior to the segment detection process so that the shear contributions from all azimuths can be taken into account. In order to avoid having to merge the shear from opposing overhead shear segments, which would add an additional step to the algorithm, a coordinate system shift is performed that allows the algorithm to run on "composite" radials made up of the radials from 0 to 180 degrees and their opposing counterparts. Because the Doppler signal from opposing radials is of opposite sign, a coordinate system shift is needed to allow the algorithm to run in the same manner whether or not it is processing data overhead.

Figure 7a is an overhead view of a microburst impacting close enough to the radar so that some of the divergent outflow passes overhead. Figure 7b plots the variation of radial velocity with range at the azimuth represented by the dotted line in 7a. As can be seen from the solid line in 7b, the velocity signature contains a discontinuity as the range passes through zero. This can be removed by simply inverting the velocity on one side of the radar, as shown by the dotted line. The radial can then be processed in the normal manner, except that the range gates lying on the inverted side of the composite radial must be scanned in order of decreasing range. To simplify the processing, the range of gate values can be thought of as varying from $-R$ to R instead of the normal 0 to R . The azimuth is varied from 0 to 180 degrees instead of 0 to 360 degrees. This is illustrated in Figures 7c and 7d. This technique does not affect the detection of non-overhead events in any way, and incurs only a small processing overhead (changing the sign of the velocity values on one side of the radar).

One additional issue that can be of concern when detecting overhead events is the quality of the velocity data at extremely close range (1-2 gates). At this range the radar receivers can still be recovering from the effects of the transmitted pulse, resulting in biased velocity values. In order to deter-

time: 92/08/08 18:59:54 1 degrees



time: 92/08/08 18:59:54 1 degrees



Figure 6. Example of a classical microburst signature. Velocity field is shown on right, with corresponding reflectivity field on left. The shear segments detected by the microburst algorithm are drawn in white.

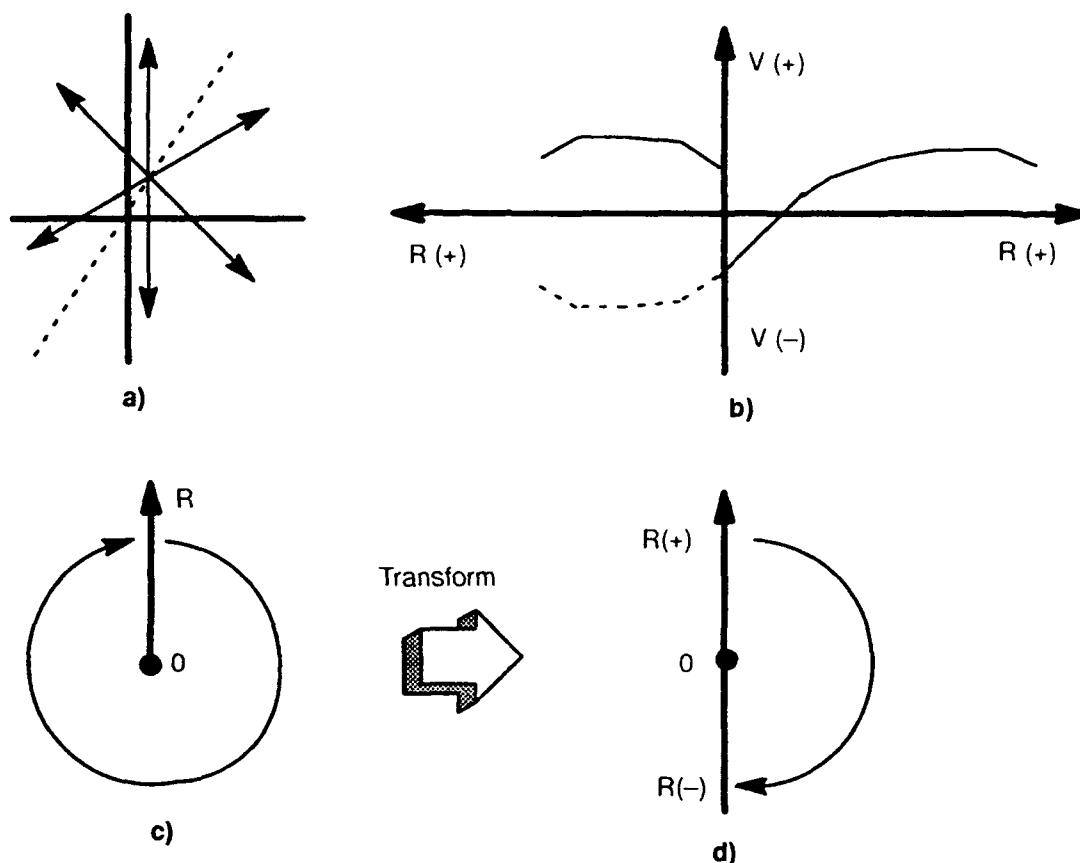


Figure 7. Coordinate System Transformation.

mine the magnitude of this problem, a study was conducted on several overhead microburst events that occurred in 1989 at the Kansas City field site. The study found that although the velocity values for the first two range gates were sometimes biased for the lower reflectivity events (< 40 dBZ), events with higher reflectivities had sufficiently accurate velocity values to allow the majority of overhead segments to be detected in their entirety. Even in the case where some of the segments are broken up into two segments (one on each side of the radar), as long as at least one unbroken segment is detected the segment association logic will still tend to group all the segments into the same cluster, providing an increased tolerance for any short range velocity anomalies. Based on these findings, the current version of AMDA has no additional processing steps to correct for possibly biased velocity values at short range. This issue is still an area of active study however, as the above findings are only valid for the transmitter/receiver chain they were tested with, and the Lincoln Laboratory ASR-9 testbed transmitter/receiver chain has been substantially modified since it was moved from Kansas City to Orlando in 1990.

Figure 8 illustrates an example of an overhead microburst, including the detected shear segments and the cluster outline that is displayed on the WSP's real-time displays. The velocity field indicates winds blowing away from the radar at all azimuths, although the velocity field is asymmetrical because the storm was moving rather rapidly to the east-northeast.

4.3 SEGMENT DETECTION

Shear segment detection can be broken down into the following steps:

1. Detect the beginning of a segment,
2. Search along radial for the end of a segment, and
3. Check the segment for validity (length, shear, slope).

4.3.1 DETECT BEGINNING OF SEGMENT

A gate is flagged as possibly being the beginning of a segment if the velocity at the following gate is higher than the current gate. There is an additional requirement that the increase between the two gates is not greater than MAX_FIRST_INCREASE (5.0 m/s). This helps reduce the number of false segments begun in noisy, low reflectivity areas.

4.3.2 SEARCH FOR END OF SEGMENT

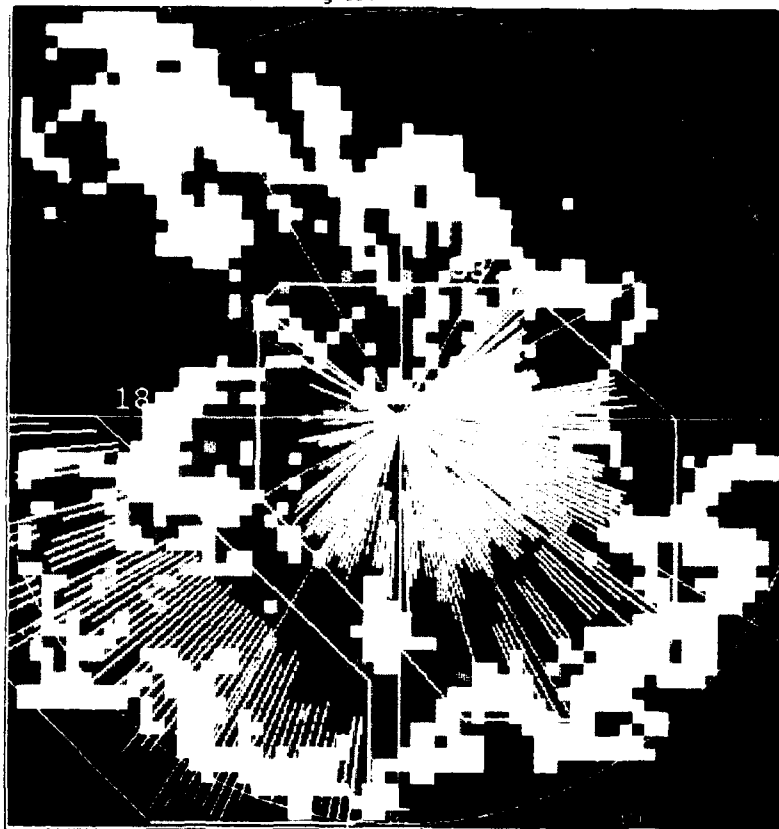
The end of a segment is signalled by one of two conditions:

- More than MAX_BAD_VALS (2) bad values encountered. Bad values can be caused by clutter breakthrough, second-trip echoes, and anomalous propagation, and are flagged as such by the signal processor prior to AMDA reading the data.
- Sum of decreases since the most recent maximum value is greater than MAX_SUM_DECREASES (5.0 m/s).

The first condition is self-explanatory. The second condition is a little more complicated, and represents the heart of the detection algorithm since it largely determines the overall length of the detected segments. As AMDA is moving from point to point along the shear segment, a variable called *sum_decreases* is used to monitor the decreasing trend of a velocity radial. This variable represents the *magnitude* of the decreasing trend, and will always be a positive quantity. The following rules are used to increase and decrease the value of the variable:

- Initialize *sum_decreases* to 0.0 at the beginning of a segment.
- When a velocity decrease is found, the magnitude of the decrease is added to *sum_decreases*. When the variable reaches or exceeds MAX_SUM_DECREASES, the growth phase of segment detection is terminated and the segment is trimmed back to the preceding maximum velocity value.

time: 91/08/09 19:43:25 1 degrees



time: 91/08/09 19:43:25 1 degrees

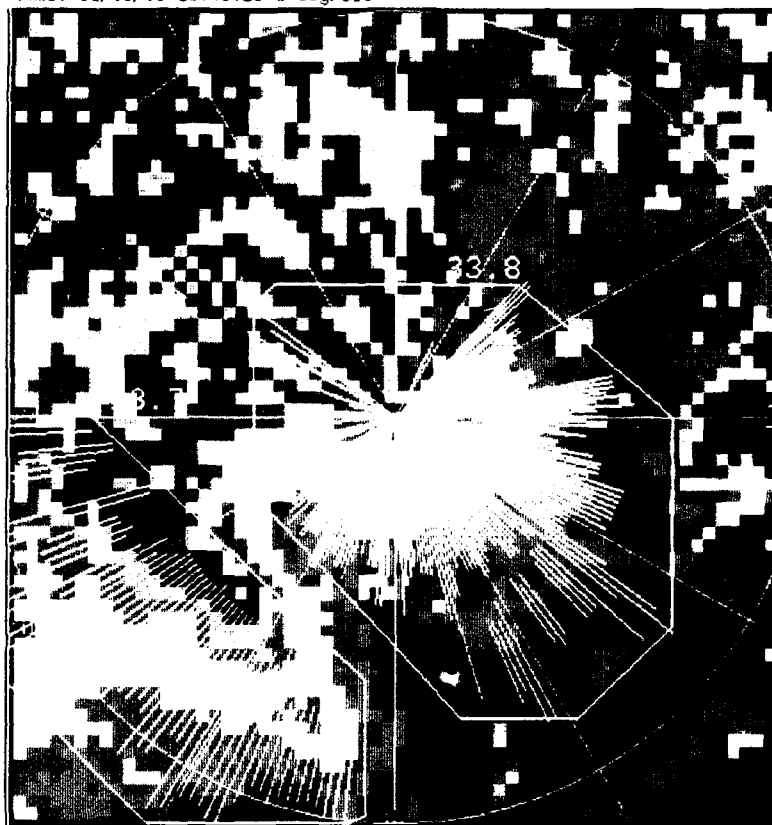


Figure 8. Detection of an overhead microburst event. Note that the velocity field (right) indicates winds blowing away from the radar at all azimuths.

- When a velocity *increase* is found, and *sum_decreases* is non-zero (recent decreasing trend encountered), then reduce the value of *sum_decreases* by *SUM_DECREASES_ADJ* (1.0 m/s), or set it to 0.0 if the result would be less than 0.0. The reason to reduce *sum_decreases* by a constant instead of the actual magnitude of the velocity increase is to weigh the decreasing trends more heavily in regions where the velocity field is oscillating up and down. This tends to terminate the growth phase of noisy segments with greater efficiency.

Figure 9 illustrates the segment growth process, including an example of how the algorithm handles a small anomaly in the velocity field. The segment is started at point A because $(V_B - V_A) > 0.0$. The value of *sum_decreases* at point B is initialized to 0.0. It remains at 0.0 until the first decrease is detected (D), at which point it is increased by the magnitude of $(V_C - V_D)$. Although the next point, E, represents an increase with respect to point D, it is not sufficient to signal a end to the decreasing trend because the velocity is still less than the current maximum value (C). Accordingly, *sum_decreases* is increased by $(V_C - V_E)$. Point F represents a slight increase with respect to point C, so *sum_decreases* is reduced by the fixed value of 1.0, to 0.8. Point G is another increase, and the decreasing trend is again reduced by 1.0, which results in the zeroing of *sum_decreases* because it cannot become negative. At this point, the algorithm has completely recovered from the velocity anomaly at point C. The segment continues to grow until it reaches point I, which represents a velocity decrease. The value of the decrease $(V_H - V_I)$ is added to *sum_decreases*, and the process is repeated for points J and K, adding $(V_H - V_J)$ and $(V_H - V_K)$, respectively. At point K, the segment growth

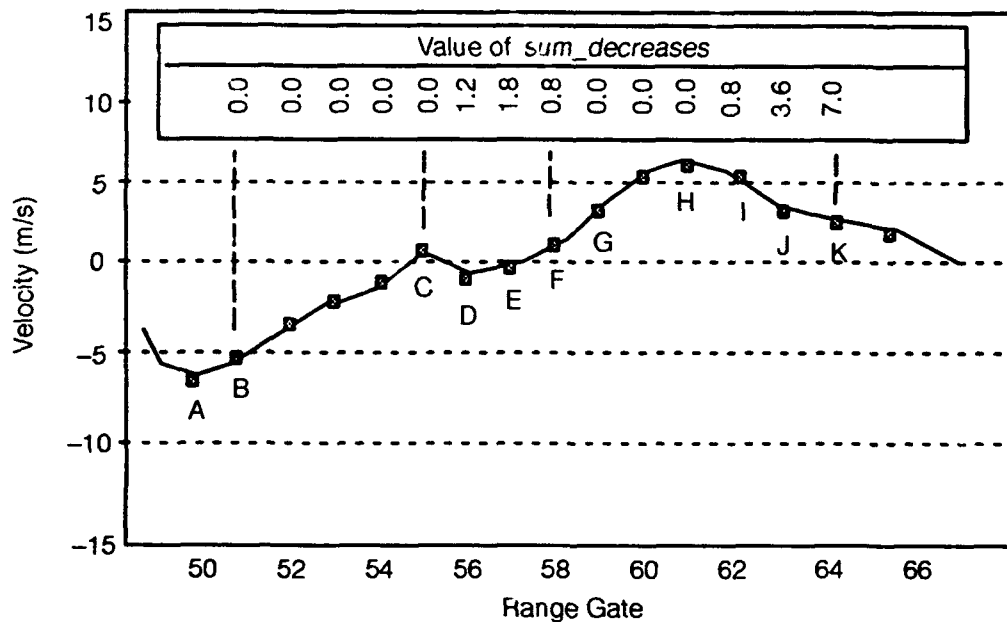


Figure 9. Segment Detection Example.

process is terminated because *sum_decreases* > 5.0 m/s. The maximum velocity value, point H in this case, is taken as the segment endpoint.

4.3.3 SEGMENT THRESHOLDING

Segment thresholding serves to remove those shear segments that are too short or too weak to have been caused by a significant divergent outflow. The segment thresholding steps are:

- Segment length must be greater than or equal to MIN_SEG_LENGTH (0.06 km).
- Segments must exhibit a differential velocity greater than or equal to MIN_SEG_SHEAR (7.8 m/s).
- The shear slope at each point in the segment must exceed MIN_SEG_SLOPE (1.8 m/s / km). A dual-window approach utilizing both an 11-point and a 7-point window (centered at the test point) is used to compute the slope, except near the endpoints of the segment where a shorter single window (9, 7, 5, or 3-point) is used due to lack of sufficient data. The slope for each of the two windows is computed using the velocity difference between the window endpoints, and the larger of the two results is taken as the final slope value. The two windows are necessary to handle the cases of longer segments where small dips or rises in a region of relatively low shear can cause a single window scheme to falsely reject a segment. This is generally not the case near the segment endpoints, and the use of only a single window in these regions has not had a negative impact.

If the slope at any point is less than the threshold, the segment is split at that point. Any segment that is split up into two or more segments must pass through the minimum length and shear tests once more to ensure segment validity.

The current value of 1.8 m/s/ km for MIN_SEG_SLOPE is somewhat lower than the 2.5 m/s/ km slope as calculated from the definition of a Microburst (10 m/s over 4 km). A setting lower than 2.5 is necessary to handle regions of shallow slope such as illustrated in Figure 2b, and the value of 1.8 has been experimentally determined to reject excessively large regions of shallow slope while retaining the regions that naturally occur within a microburst.

The slope check thresholding test is the most computationally intensive of the three thresholding steps, and for that reason the segment length and strength tests are run first. The great majority of invalid segments will be filtered out by the first two tests, thereby reducing the number of segments that require the slope check.

4.4 SEGMENT TEMPORAL SMOOTHING

The ASR-9 antenna scans once every 4.8 seconds, providing an opportunity to temporally smooth the shear segments to decrease the scan-to-scan variability. In the AMDA implementation, every segment has associated with it a variable called *seg_age*, which starts out at a value of 1 when the segment is first detected. For each successive scan on which the segment is present (determined by overlap), *seg_age* is incremented by 1, until it reaches a maximum value of MAX_SEG_AGE (7). For each scan where the segment is missing, *seg_age* is decreased by 1. A segment is automatically inserted (coasted) into a scan if *seg_age* \geq MIN_SEG_AGE_INSERT(3) and the segment is missing from the current scan.

Figure 10 shows the results from a Monte-Carlo simulation of the above algorithm for three different "segment present" percentages. From the graph, it can be seen that for segments present on only 25 percent of the scans, the probability that *seg_age* reaches 3 is quite small, resulting in the insertion of coast segments roughly 3 percent of the time. For segments that are present 50 percent of the time, coast segments will be created 58 percent of the time, and when segments exist on 75 percent of the scans, a coast segment will be inserted 98 percent of the time. The segment age requirement of 3 was chosen because of the combination of a small percentage of 'false' insertions, and a high percentage of 'true' insertions.

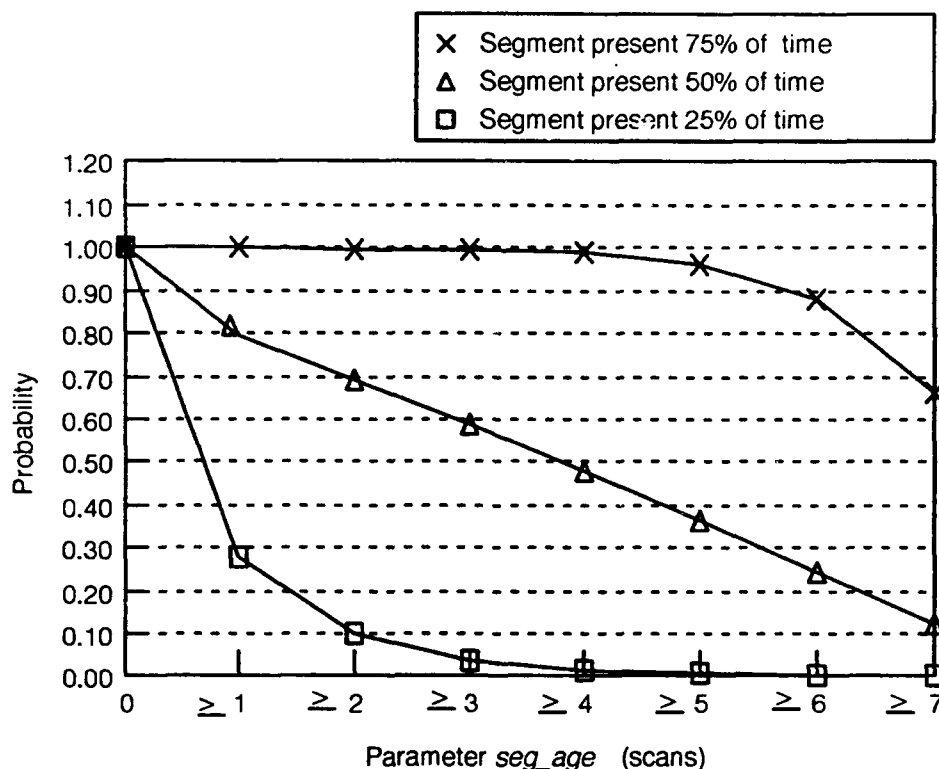


Figure 10. Probability Distribution of Parameter *seg_age*.

The above argument is directed toward the case where a given segment is flickering on and off because it is near one of the thresholds. Another case to consider is that of a point target (aircraft) causing a segment miss on several consecutive scans. Assuming that the segment had been fairly steady just prior to the point target and *seg_age* had reached the maximum value of 7, a coast segment would be created for up to four (7-3) scans in which the segment was missing. This corresponds to $4 \times 4.8 \text{ seconds/scan} = 19.2 \text{ seconds}$ of enhanced segment continuity, which is adequate when compared with the time a typical moving point target will remain within a radial.

4.5 SEGMENT ASSOCIATION

Segment association is done in a manner similar to the TDWR algorithm. Segments on neighboring radials are tested for range overlap, and grouped together into "clusters" when overlap occurs. There are three main steps in the grouping process.

1. Using an "azimuthal association window," determine if two segments are close enough in azimuth to be subjected to the range overlap test.
2. If so, begin a new cluster when the segments also overlap each other in range.
3. Continue to grow the cluster until no more overlapping segments are encountered within the azimuthal association window.

The TDWR algorithm utilizes a fixed azimuthal association window (usually 2 deg.) when performing segment association. In the case of the ASR-9, which must detect microbursts at close range owing to on-airport location, nearby point targets or ground clutter can often obscure a larger azimuthal region than those at greater distances. This situation is depicted in Figure 11a. To address this problem, the AMDA approach is to make the azimuthal association window a linear function of range (The range is determined from the midpoint of the segment under consideration). The maximum and minimum limits of the window size are specified as variable site parameters (See Appendix A for full parameter names). The maximum window size is typically set at 15.4 deg. at zero range, ramping down to a minimum value of 4.2 deg. at a range of 10.0 km (Figure 11b). These parameters are generous when compared with the TDWR setting of 2 deg., and it is true that these settings will result in some clusters containing only widely scattered segments at close ranges. There is an additional AMDA processing step, segment density thresholding, to address this issue, and the explanation is deferred to that section.

The overlap test simply tests if the inner *SEG_OVERLAP_PERCENTAGE* (50 %) of neighboring segments have any overlap. During AMDA optimization experiments, this overlap requirement has been varied between 25 percent, which tended to fragment segments from the same microburst into different clusters, and 75 percent, which tended to group segments from multiple microbursts into a single cluster. The value of 50 percent appears to be a good compromise between these two extremes.

To be considered valid, clusters must contain at least *MIN_CLUSTER_SEGS* (4). If this is true, then the cluster is passed on to the reflectivity thresholding module.

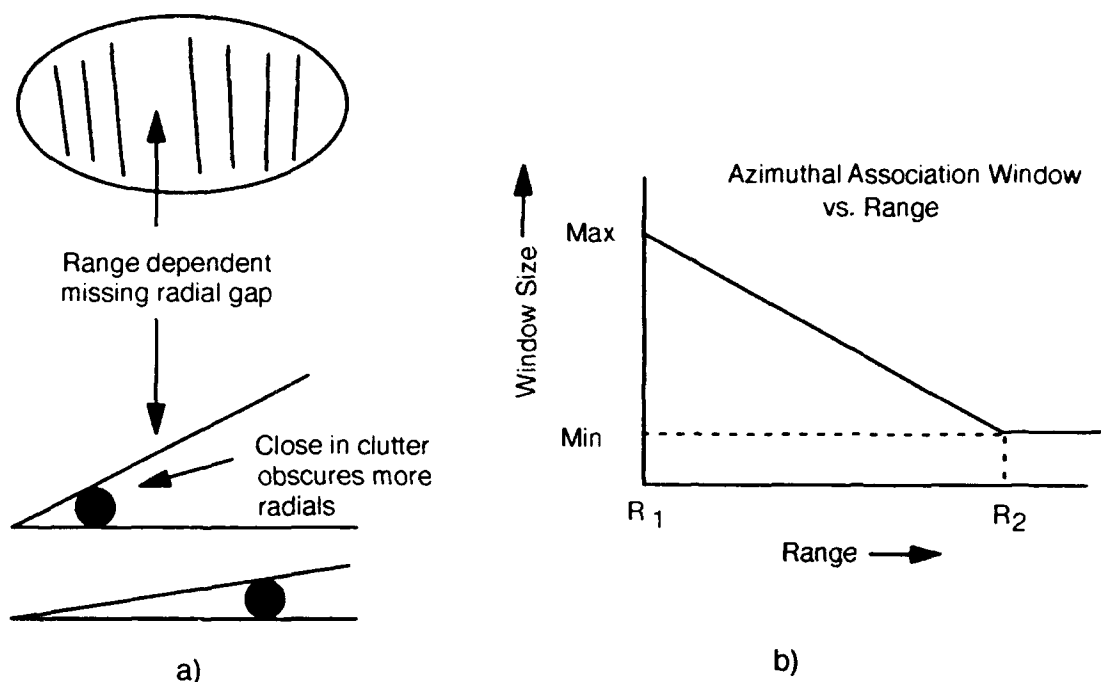


Figure 11. Association Criteria Range Dependence.

4.6 REFLECTIVITY THRESHOLDING

The ASR-9 dual-beam velocity estimator may not reliably predict the low-level radial velocity field in all meteorological situations. Analysis of data acquired in Huntsville, AL and Kansas City, KS revealed that shear segments located primarily on the fringes of storm cells were a major source of false alarms, most often due to errors in the dual-beam velocity field at these locations. In the majority of cases, overhanging precipitation had contaminated the power spectrum in excess of the dual-beam algorithm's ability to compensate, causing the erroneous velocity values. An example of this type is presented in the performance evaluation section of this report. Since the situation occurs most frequently at the edges of storm cells, AMDA includes a reflectivity-based thresholding step to filter out this type of false alarm.

The reflectivity thresholding process is illustrated in Figure 12. First, segments with greater than REFL_THRESH_LENGTH_PERCENT (50%) of their length lying within "core" reflectivity (\geq REFL_THRESH_CORE_DBZ (40 dBZ)) are marked as valid microburst segments. Next, to reduce the chances of discarding shear segments associated with a true microburst, any other segments that lie within REFL_THRESH_DIST (0.5 km) of a valid segment, as measured between the two segment mid-points, are also marked as valid. All other segments in the cluster are discarded.

The reflectivity thresholding process significantly reduces the false-alarm rate in the environments studied thus far. A typical case illustrating the effect of the thresholding is shown in Figure 13. In this case, a divergent signature is clearly present in the velocity field (right) and a cluster of seg-

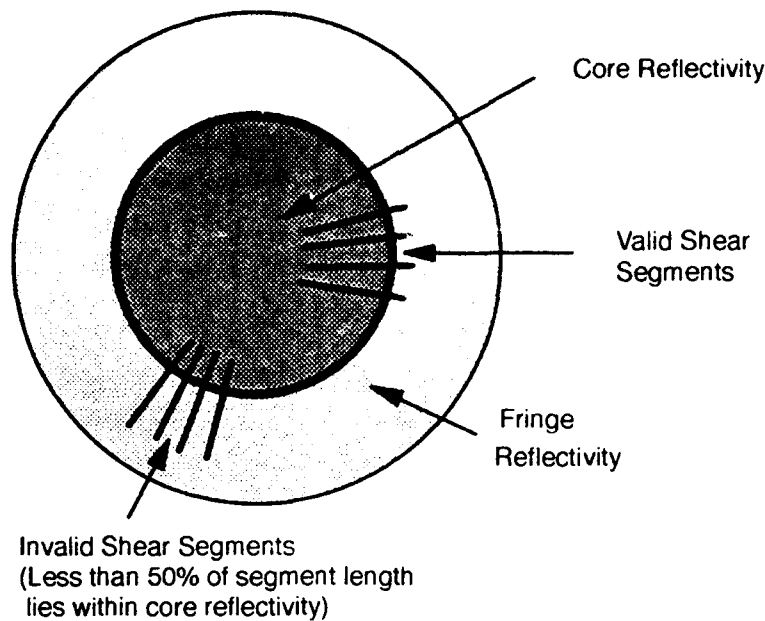


Figure 12. Reflectivity Thresholding of Shear Segments.

ments (6) that passes the area and strength thresholds is present. However, examination of the reflectivity field (left), indicates that the majority of the segments are located in a region of low reflectivity, and are potentially invalid. Four out of the six segments were in fact rejected by the reflectivity threshold, and the remaining segments were insufficient to qualify as a microburst. Subsequent analysis of this case showed the receding portion of the velocity signature was being caused by precipitation aloft, and the reflectivity threshold had successfully eliminated a false alarm.

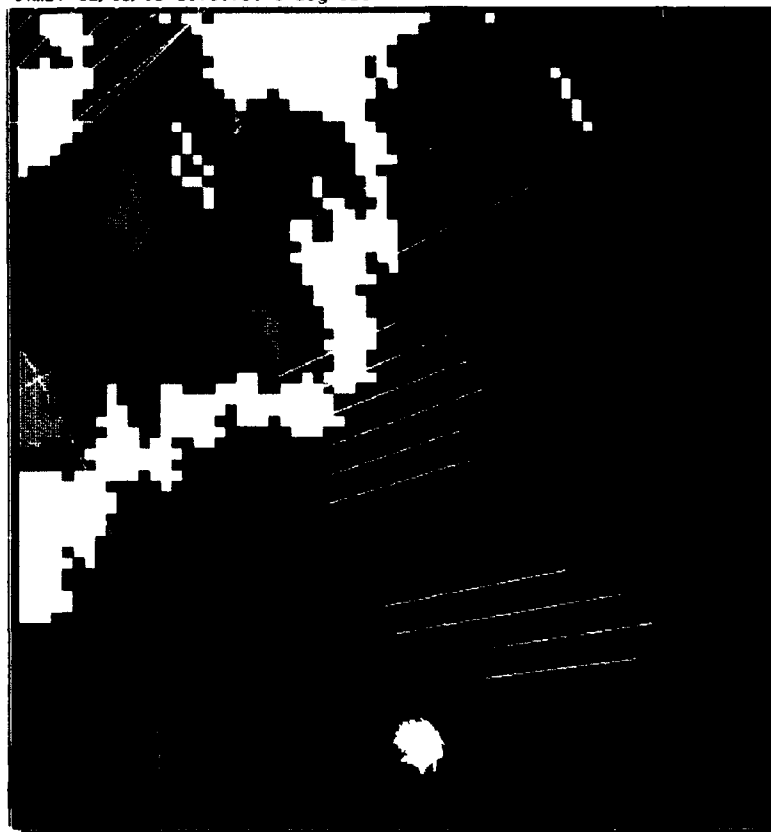
In a dry environment, the outcome of using this method remains to be seen, and the algorithm will probably need modification in order to avoid the rejection of dry events occurring simultaneously with events containing higher reflectivities. One possibility currently being evaluated is to determine the core reflectivity threshold on a storm-cell by storm-cell basis instead of utilizing a single threshold for the entire scan. Improvements to the dual-beam algorithm are also expected to reduce the overall need for reflectivity thresholding.

4.7 SEGMENT DENSITY THRESHOLDING

In the description of the initial segment association step, we mentioned that the relatively large radial gap allowed between associated segments could result in large clusters with only a sparse number of segments. There are actually four cases to consider.

The first case, shown in Figure 14a, is that of the ideal cluster, with no missing segments. This case needs to be passed unaltered through the segment density thresholding process. The second case, Figure 14b, is that of a cluster with multiple missing segments, but with a high density of contiguous detections in the regions neighboring the missing segment gap. The most common causes of

time: 92/08/08 19:00:50 1 degrees



time: 92/08/08 19:00:50 1 degrees



Figure 13. Reflectivity thresholding successfully eliminating a false alarm on the fringe of a storm cell. The group of segments in this case met all the microburst area strength requirements, but failed the reflectivity threshold.

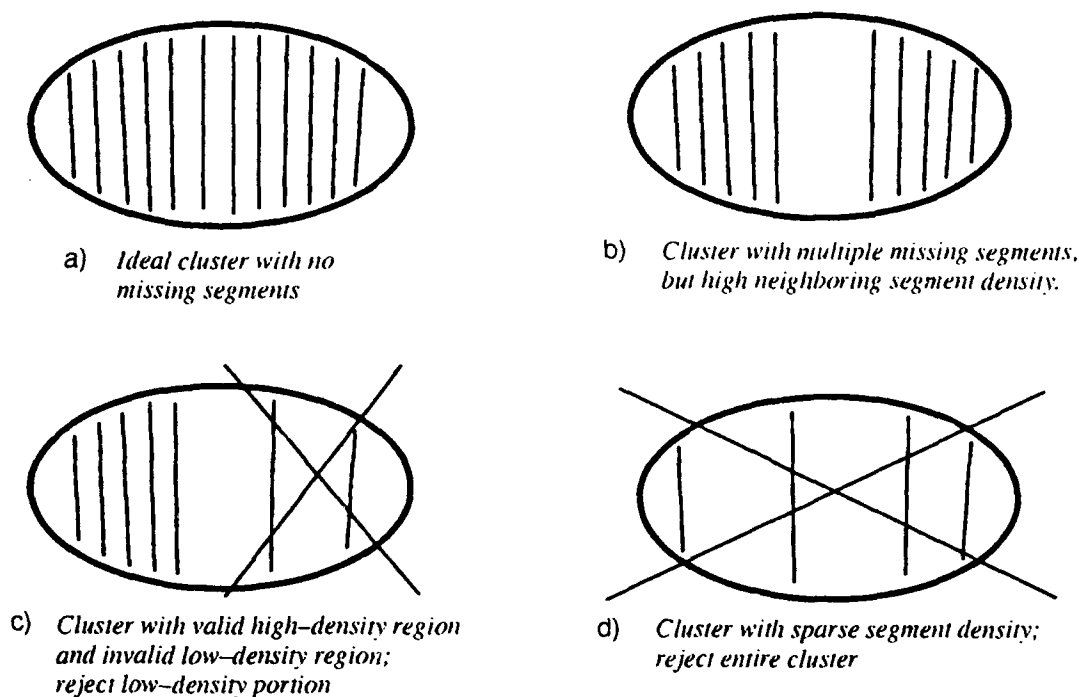


Figure 14. Typical Segment Density Distributions and Associated Clustering Decisions.

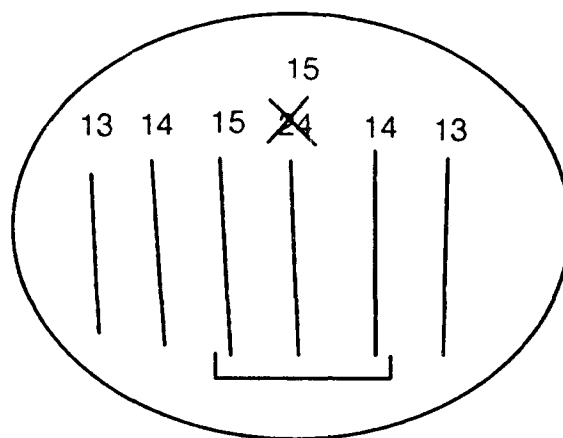
this condition are ground clutter and point target contamination. It is desirable to accept cases such as this as a valid cluster. The third case, Figure 14c, consists of a cluster with a region of high segment density, and also a low density region. The desired action in this case is to trim off the low density region while retaining the high density region. The fourth case, Figure 14d, is that of a cluster that contains a very sparse distribution of segments, in which case the entire cluster should be rejected.

To achieve the desired density thresholding behavior, AMDA utilizes a sliding window of width $[(\text{AZIMUTH_GAP}(\text{Range}) \times 2) + 1]$ to compute the segment density at each radial. The azimuth gap is the same as that used in the segment association process, and is a function of range. The sliding window is always centered on the segment being evaluated, so the window size near the cluster edges must be reduced if necessary to avoid extending beyond the cluster azimuth limits. For example, the window size for the second and third azimuth positions in a cluster is limited to three and five radials, respectively. No test is performed on the edge segments themselves. The segment density is simply calculated as the percentage of segments present in the window, and must be greater than or equal to SEG_DENSITY_THRESH (50%) or the cluster is split at that point. All resulting sub-clusters are then required to meet the minimum segment requirement of CLU_MIN_SEGS(4), or they are discarded.

4.8 CLUSTER SHEAR DETERMINATION

Even with the spatial filtering and data consistency checks performed up to this point, it is still possible to encounter occasional shear segments with spurious values. This is obviously undesirable

when estimating the overall shear of the cluster, because the overall shear is normally defined as the maximum value across all shear segments, and a single outlier can dramatically influence the maximum value. On the other hand, smoothing the shear values excessively will result in the loss of the true detected maximum shear. AMDA uses a 3-point median test to check through the segments, and replace any detected outliers with the median of the shear from the surrounding three-point window (Figure 15). This process will remove most outliers, while retaining the true maximum shear value in the majority of cases. Subsequent to the median filter, the cluster shear is set equal to the maximum shear value across all segments in the cluster.



If shear value of a segment is more than 20 percent higher than the median of the three-segment window, replace shear value with median value.

Figure 15. Shear Magnitude Outlier Rejection.

4.9 AREA THRESHOLDING

The purpose of area thresholding is to remove clusters of segments which, because of their small size, are probably not true microburst events. This is not a trivial problem, as some of the stronger microbursts are initially very compact, and it is essential to avoid filtering out these microbursts while attempting to improve the overall false-alarm rate. To help alleviate the problem, it is useful to note the relationship between Probability of False Alarm (PFA) and shear magnitude. Figure 16 is a plot of PFA vs. shear magnitude using the average of the 1991 and 1992 scoring results presented in Section 5 of this report. As seen in the figure, the likelihood of a cluster being a false alarm decreases rapidly with increasing shear magnitude. This information can be used to advantage in the area thresholding process by using a threshold that is inversely proportional to shear magnitude.

A second consideration is that of asymmetrical microbursts, when the percentage of microburst area detected can sometimes decrease with decreasing range. As an asymmetrical microburst (with major axis perpendicular to the radar beam) nears the radar, the viewing angle of the radar renders some of the velocity signature of the microburst invisible, due to the geometry. This is illustrated in

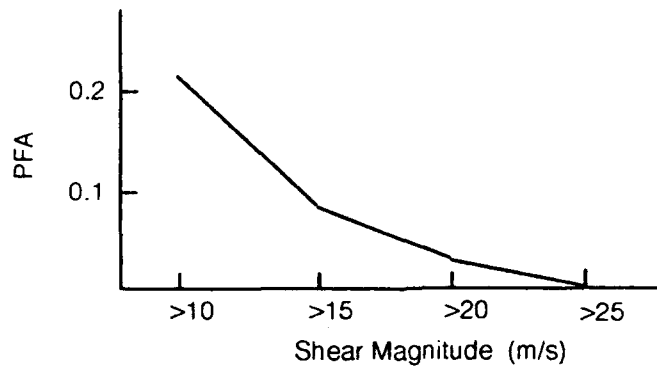


Figure 16. Probability of False Alarm vs. Shear Magnitude.

Figure 17. When the microburst is relatively distant (left), the radar “sees” almost the entire region of shear, but as the microburst moves closer to the radar (right), the radial component of the shear decreases at the wider angles, and some of the segments are not detected because the shear falls below the detection threshold.

The previous considerations can be utilized effectively by making the area threshold a function of both cluster shear strength and range. The relationship used by AMDA is shown in Equations 1 to 3. The parameters used in the equations are defined as follows (current settings in parentheses):

| | |
|----------------------------|---|
| $Area_{min}$ | Absolute minimum area threshold (0.5 km ²) |
| R_{min}, R_{max} | Minimum and maximum range boundaries (2.0, 16.0 km) |
| $Shear_{min}, Shear_{max}$ | Minimum and maximum shear boundaries (7.8, 27.5 m/s) |
| R_{slope} | Rate of change of area threshold with respect to range (0.1km ² /km) |
| A, B, C | Area threshold shear correction coefficients (30.0, 2.5, -1.0) |

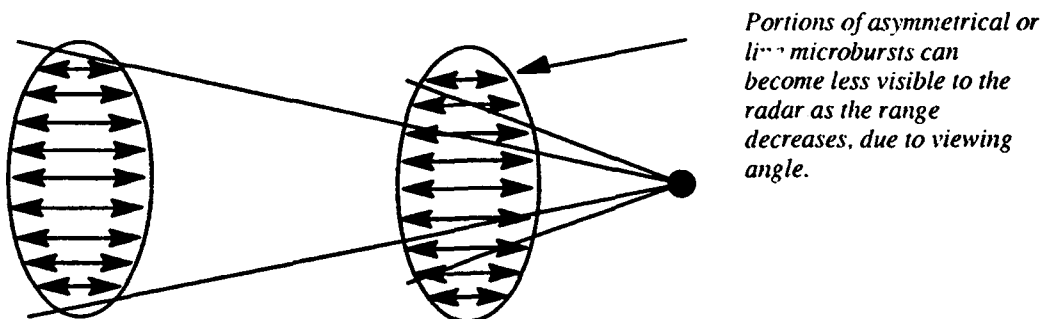


Figure 17. Detected Microburst Area vs. Range.

Note that the parameter names are not the full symbolic names (i.e. CLU_MIN_AREA) used in the algorithm parameter file. The complete list of symbolic parameter names can be found in Appendix A.

The area threshold for a given cluster of segments is computed using the sum of an absolute minimum area threshold and two correction terms:

$$Area_{thresh} = Area_{min} + \Delta Area_{range} + \Delta Area_{shear} \quad [1]$$

The range correction term is computed using a simple linear relationship with one adjustable parameter, R_{slope} , and has the effect of increasing the area threshold vs. range.

$$\Delta Area_{range} = R_{slope}[R - R_{min}] \quad [2]$$

The shear correction term is calculated using a non-linear equation designed to match the shape of the PFA vs. Shear Magnitude curve. This term is small for strong events, but increases rapidly as the event strength decreases.

$$\Delta Area_{shear} = \frac{A}{(Shear + B)} + C \quad [3]$$

The two correction terms are both prevented from becoming negative or excessively large by bounding the independent variable in each case. The limits are shown below.

$$R = \begin{cases} R, & R_{min} < R < R_{max} \\ R_{min}, & R < R_{min} \\ R_{max}, & R > R_{max} \end{cases} \quad Shear = \begin{cases} Shear, & Shear_{min} < Shear < Shear_{max} \\ Shear_{min}, & Shear < Shear_{min} \\ Shear_{max}, & Shear > Shear_{max} \end{cases}$$

The parameter settings shown above were determined in an iterative manner, whereby single parameters were varied in turn, and the algorithm scoring results were examined. At a range of 2km, the current settings result in an area threshold that ranges from 0.5 km² for very strong events (>27.5 m/s) to 2.5 km² for the weakest events (7.5 m/s). A contour plot illustrating the operational area thresholds (boldface – in square kilometers) is provided in Figure 18. Because the microburst area distribution is sensitive to changes in other parameters, especially the allowed radial gap, the area thresholding parameters must be re-optimized when other parameters are changed.

4.10 CLUSTER TEMPORAL SMOOTHING

To provide a more consistent microburst appearance from scan to scan, a simple temporal filter is utilized. To prevent spurious clusters from being output as valid microbursts, a cluster must be present on three successive scans to be declared valid. This introduces a 10 second latency period in the initial detection phase, but because microbursts are almost always detected in their growing stage, this amount of latency is not viewed as a serious problem. To reduce the amount of microburst “flickering” that can occur while an event is dying out, microbursts are “coasted” for a maximum of 12 scans (1 minute). This tends to increase the overall false-alarm rate slightly because false alarms are,

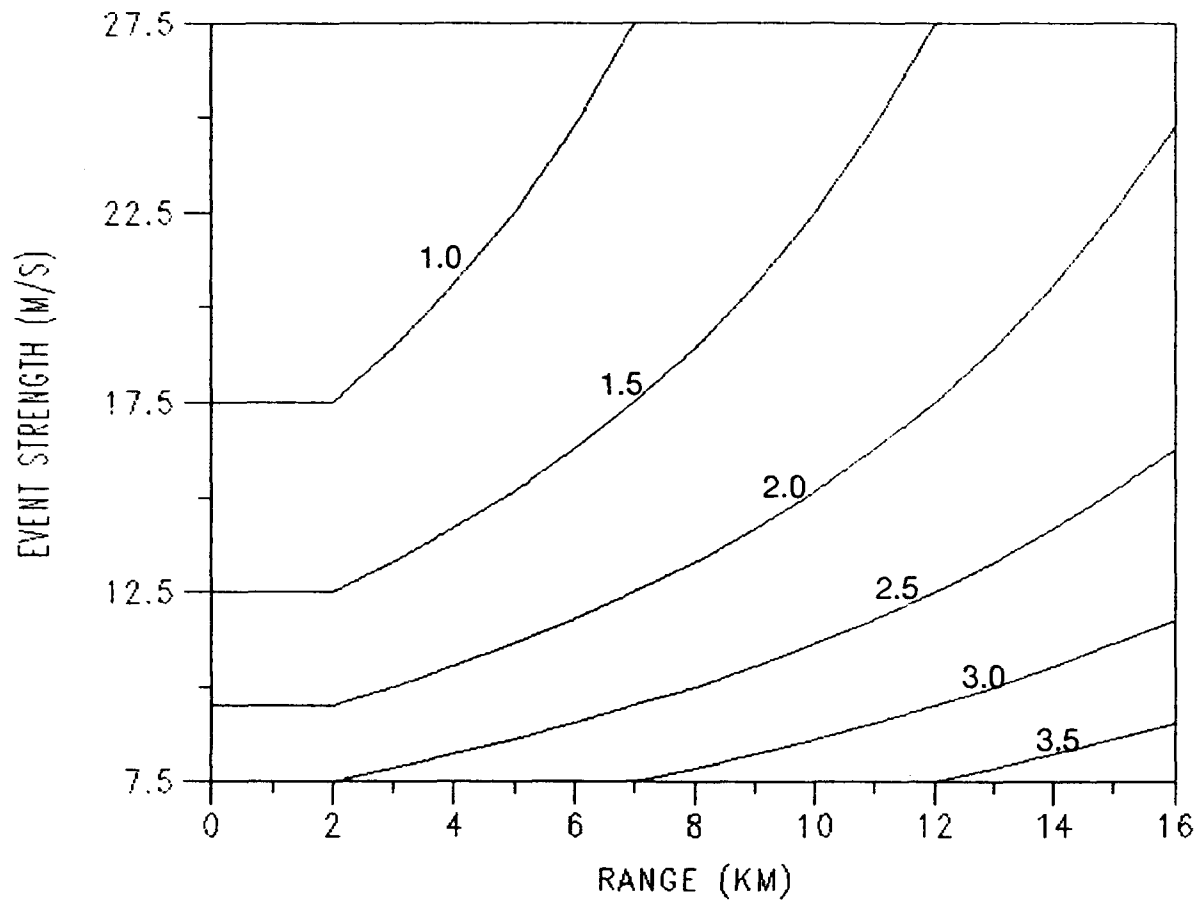


Figure 18. AMDA Area Thresholding.

in effect, "amplified," but this minor FAR increase is preferable to providing ATC with an inconsistent display.

4.11 SHAPE ALGORITHM AND FINAL OUTPUT

The temporal smoothing of clusters is the final step of the microburst algorithm that is specific to the ASR-9. From that point, microburst warnings, along with the segment clusters for each microburst, are sent to the shape algorithm [Wilson, 1992] running on a Sun Workstation. This algorithm, identical to the algorithm used by TDWR, creates "band-aid" shape(s) for each microburst, which are then sent with the microburst shear value to the Geographical Situation Display (GSD) in the Control Tower. An example of the GSD display is shown in Figure 19.

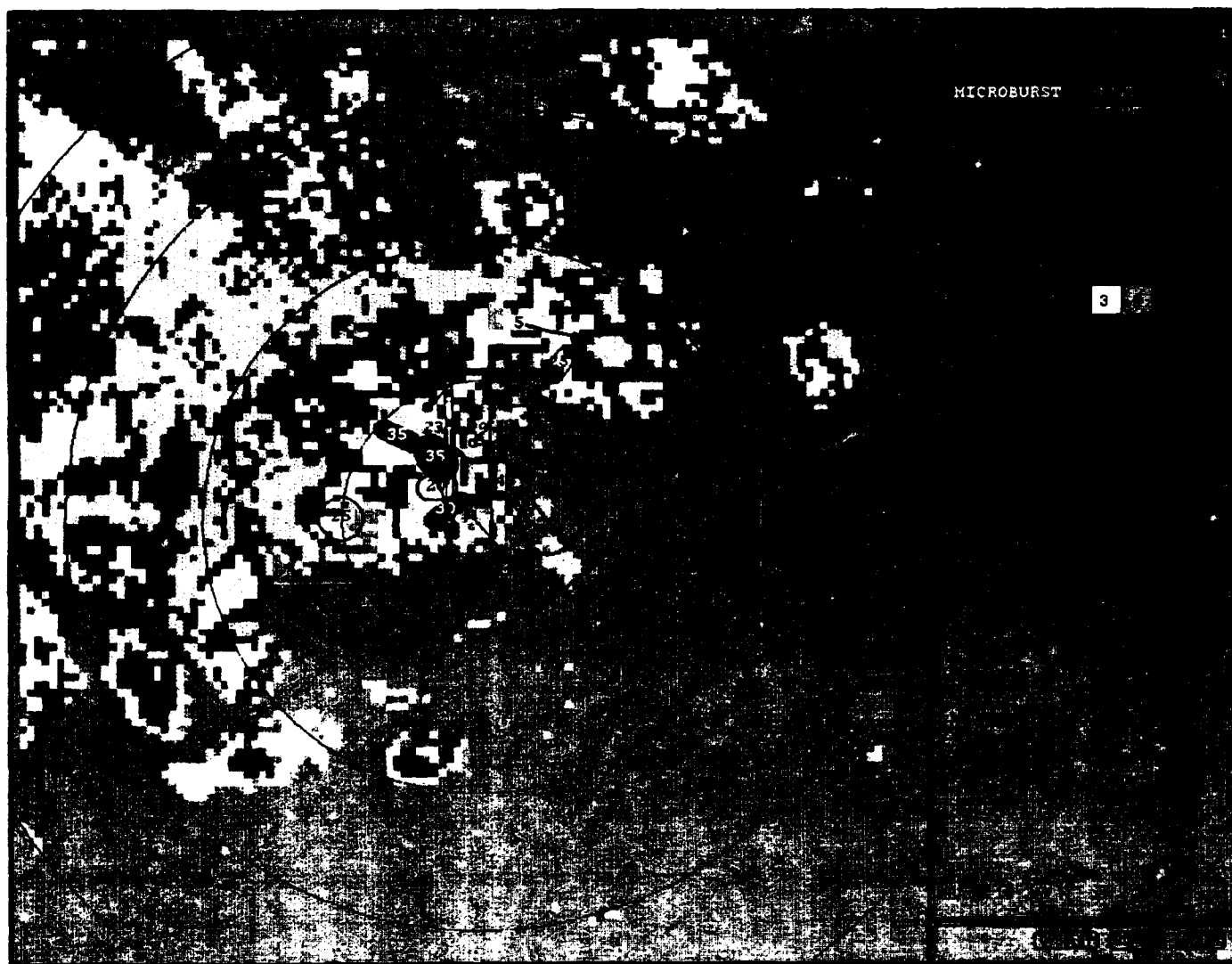


Figure 19. Geographic Situation Display. Filled red circles are detected microbursts with the measured wind changes across the event (in knots) indicated. Open red circles show divergent outflows with measured wind changes less than 30 knots ("wind shear with loss"). Purple arc is a detected gust front with the estimated location of the front 10 and 20 minutes in the future indicated by dashed purple lines; an estimate of the wind speed and direction behind the front is given by the purple vector. Six levels of precipitation reflectivity are shown and the speed and direction of storm movement is given by the black vector and associated number. The blue arrows and numbers show the wind speed and direction measured by LLWAS anemometers.

5. MICROBURST ALGORITHM PERFORMANCE EVALUATION

5.1 EVALUATION STRATEGY AND RESULTS

Signal-processing and meteorological detection algorithms for the ASR-9 WSP have been developed and validated using data collected in Huntsville, AL, Kansas City, KS and Orlando, FL with the Lincoln Laboratory testbed. This section discusses the performance of the "mature" version of the ASR-9 Microburst Detection Algorithm (AMDA), using data from eleven active weather days during the 1991 Orlando operational test, and ten active weather days during the 1992 test. AMDA output was scored against corresponding "truth" data from the TDWR pencil-beam radar located approximately eight kilometers south of the Orlando ASR testbed. Truth data were generated by examining TDWR low-level PPI scans taken at one-minute intervals during the active periods. Using truthing software, locations (polygonal outlines) and intensities of microbursts were entered into a computer file. An automated scoring program then compared the locations of all ASR alarms within 30 seconds of a truth time with the locations of true events at that time, scoring an alarm a "hit" if it overlapped a truth region, and a "false alarm" if it did not. Truth events that were not intersected by an ASR alarm were scored as "misses." Since the majority of TDWR low-level scans were "sector" scans centered over the Orlando International Airport, azimuthal limits were included in the truth files and applied by the automated scoring program so that only alarms within the region of available truth data were scored. An alarm which lay partially within the azimuthal bounds was not scored unless it intersected a truth outline, in which case it was considered a hit.

Scoring results for 1991 and 1992 are presented in Tables 1 and 2. It is important to note that this end-to-end evaluation of WSP microburst detection capability was highly dependent upon the accuracy of base data generated by the signal processing algorithm. Probability of Detection (POD) and Probability of False Alarm (PFA) are indicated as a function of microburst intensity (DELTAV) in meters/second. The statistics are cumulative from right to left. Denominators in the two ratios were, respectively, the total number of truth observations and ASR alarms in the scored data set. Thus, for microbursts located within the operationally significant near-airport zone extending 8 kilometers (5 miles) from the ASR and possessing maximum deltav of at least 15 m/s (30 knots), the ASR-WSP system was greater than 95 percent successful in detecting the events. The corresponding PFA's were seven and 10 percent, respectively, for the two years. Significantly larger false-alarm probabilities occur for divergent outflows weaker than 15 m/s. Fortunately, false alarms in this category are of less concern than those for stronger outflows because 1) most pilots will choose to continue a landing or take-off when given a "wind shear with loss" alert generated by these weaker events, and 2) Orlando microbursts are often slightly asymmetric, causing legitimate discrepancies in observed velocity differentials between the ASR and truth radar. In the latter case, false alarms and microburst misses occur frequently if one radar observes weak microburst-strength shear (slightly above 10 m/s within 4 km) while the other radar observes below-microburst-threshold shear. Another statistic provided in Tables 1 and 2, Shear Ratio (SR), was the mean difference in intensity of the true events as seen by the ASR-WSP system versus the truth radar. Thus, for microbursts stronger than 25 m/s (50 knots), the ASR-WSP system typically underestimated the maximum divergence by approximately 5 m/s

(10 knots). It should be noted, however, the AMDA measure of maximum divergence occurs along a single azimuth, but the human "truth" might consider multiple azimuths when assigning strengths to truth events.

Table 1.
Hit-Miss Scoring Results for 1991 Orlando Test

| PERFORMANCE STATISTICS BY DELTAV (m/s) OUT TO 8 km | | | | |
|--|------------------|------------------|------------------|------------------|
| | ≥ 10 | ≥ 15 | ≥ 20 | ≥ 25 |
| POD | 5447 / 5900=0.92 | 4026 / 4129=0.98 | 2424 / 2429=1.00 | 1051 / 1052=1.00 |
| FAR | 1343 / 8586=0.16 | 427 / 5863=0.07 | 46 / 2865=0.02 | 0 / 1040=0.00 |
| SR | 1.44 | -0.40 | -2.23 | -4.11 |

Table 2.
Hit-Miss Scoring Results for 1992 Orlando Test

| PERFORMANCE STATISTICS BY DELTAV (m/s) OUT TO 8 km | | | | |
|--|------------------|------------------|------------------|------------------|
| | ≥ 10 | ≥ 15 | ≥ 20 | ≥ 25 |
| POD | 5317 / 6079=0.87 | 3776 / 3935=0.96 | 2018 / 2067=0.98 | 1011 / 1037=0.97 |
| FAR | 2251 / 8534=0.26 | 489 / 4981=0.10 | 5 / 1915=0.00 | 0 / 617=0.00 |
| SR | 0.78 | -0.82 | -3.33 | -5.46 |

An alternate scoring technique, known as path-oriented scoring, utilized dual-Doppler wind measurements to indicate the wind shear loss/gain that would be experienced by aircraft along the runways and their respective approach or departure corridors. The TDWR and University of North Dakota (UND) radars were the sources of the dual-Doppler truth. This type of scoring provided a more critical evaluation of ASR-WSP performance because favorable scoring results required highly accurate detection of event location and strength along these narrow "corridors." The losses indicated by the truth were compared to those issued by the ASR-WSP system on nine days during 1991 operations, and yielded the results in Table 3. Here, $P(\text{Loss}|\text{Loss})$ represents the probability the ASR-WSP issued a loss alert (wind shear with loss less than 30 knots) or microburst warning (microburst with loss greater than 30 knots) for a true loss of less than 30 knots. Similarly, $P(\text{Loss}|\text{MB})$ indicates the probability the ASR-WSP issued a loss alert or microburst warning given there existed a loss *greater* than 30 knots, and $P(\text{MB}|\text{MB})$ gives the probability a microburst warning was declared for these same conditions. $PFA(\text{MB})$ was the probability the ASR-WSP issued a microburst warning when no loss was evident in the dual-Doppler truth. $PFA(\text{Loss})$ gives the probability the ASR-WSP declared a microburst warning or loss alert under the same circumstances. $P(\text{OW})$, or "overwarning," was the probability a microburst warning was given when dual-Doppler data revealed a loss

alert was more appropriate. These results are similar to those produced by the hit-miss strategy. Slightly lower detection probabilities resulted from the aforementioned ASR-WSP underestimates of the stronger divergences, and by the more rigorous requirements of this scoring method. Differences in the two scoring method statistics emphasize leniencies in the hit-miss scoring method, such as rewarding full detection for partially-observed or grossly over or underestimated (intensity) events.

Table 3.
Path-Oriented Scoring Results for 1991 Test

| Detection Probabilities | | False-Alarm Probabilities | |
|-------------------------|------|---------------------------|------|
| P (Loss/Loss) | 0.72 | PFA (MB) | 0.05 |
| P (Loss/MB) | 0.97 | PFA (Loss) | 0.10 |
| P (MB/MB) | 0.84 | P (OW) | 0.26 |

5.2 INVESTIGATION OF ALGORITHM FAILURES

Occurrences of ASR-WSP false alarms and missed microbursts in the scored data were identified by overlaying single-Doppler-based truth polygons and ASR-WSP alarms over images of the corresponding ASR and TDWR (or UND) surface radar data. This practice often led to discovery of the cause of a false alarm or miss. For example, an ASR-WSP false alarm bounding a region of divergence clearly visible in the ASR velocity field, but not evident in the corresponding region of the nearest TDWR velocity data, prompted a comparison of the ASR and TDWR reflectivity fields within the alarm region, often revealing substantially larger areal coverage of precipitation in the ASR data. This suggested the five-degree-wide beam of the ASR was observing elevated reflectivity structures in these cases, and this was verified by subsequently examining true or synthesized RHI data through the area of interest. In the color plots that follow, alarms generated by the ASR-WSP are represented by white polygons, and divergence segments (azimuthal lines along which significant divergence existed in ASR data) are represented by white segments. Locations of truth events are indicated by red polygons. In Figure 20, a fast-moving gust front (note velocity folding in C-band TDWR data) spawned by storms west of the airport initiated new cell growth southeast of the ASR, immediately behind the frontal boundary. Velocity data show the ASR (upper right) observed a 22.7 m/s maximum loss centered seven kilometers east-southeast of the radar, while the TDWR (lower right) saw only slight divergence at that location. Of particular note is the presence of approaching (negative) velocities within the alarm region in the ASR data. A comparison of the reflectivity fields (left-hand panels) associated with the alarm shows far less signal return in the TDWR data (lower left). A synthesized RHI scan (Fig. 21) created from TDWR volume scan data through the alarm region revealed easterly winds existed within an elevated reflectivity core (situated above folded velocities associated with the fast-moving gust front), while surface winds were

westerly due to the gust frontal passage. The ASR was sensitive to the easterly (inbound) motion because of its wide beamwidth. Thus, this is an example in which physical characteristics of the ASR led to issuance of false microburst warnings by the microburst detection algorithm.

The ASR-9 Microburst Detection Algorithm's use of "noisy" velocity estimates in regions of low signal return also led to issuance of false alarms. Large-magnitude velocity estimates sometimes occurred in ASR range bins in areas of low signal return, and the incorporation of these estimates by the detection algorithm produced fictitiously high divergences. Figure 22 illustrates this occurrence. The -9 to -12 m/s velocities in the ASR velocity field (upper right) within the 20.7 m/s alarm were used by the detection algorithm even though they corresponded to relatively low reflectivity values (upper left). The nearest corresponding TDWR data (bottom panels) and UND data (not shown) confirmed microburst-strength shear was not present in the alarm region. (Comparison of the ASR and TDWR reflectivities suggests that elevated-core syndrome may also have contributed to the ASR surface velocity overestimates in the positive velocity portion of this alarm.) Possible fixes for this problem include improving the ASR Dual-beam Processing Algorithm, or rejecting velocity estimates associated with low-reflectivity values (e.g. less than 20 dBZ).

Strength and range-dependent area thresholding parameters employed by the microburst algorithm resulted in occasional microburst misses, mainly early in the lifetimes of microbursts when they were quite small upon initial impact with the ground. An example of this occurrence is provided in Figure 23. A true microburst signature was evident in the ASR data (top panels) within the 17 m/s truth polygon, but the detection algorithm did not issue an alarm because the area of the "cluster" of divergence segments was slightly less than the required 1.5 square kilometers for an event at that range and of this intensity. An alarm was issued by the detection algorithm a few seconds later. The corresponding TDWR truth data is shown in the bottom panels. Short delays in microburst detection were also caused by cluster age requirements imposed by the microburst detection algorithm, as alarms were not declared until a cluster was valid for three consecutive scans. Conversely, false alarms occasionally resulted from AMDA's coasting of alarms after a cluster disappeared.

Microburst asymmetry accounted for some of the false alarms and microburst misses tabulated in the ASR-WSP performance scoring. Occasionally a microburst was visible in the ASR data, but not in the TDWR data, when the ASR had a more favorable viewing angle for an asymmetric event. These events were inappropriately scored as false alarms because single-Doppler (TDWR) data was used as truth. Figure 24 depicts this occurrence. Both ASR (upper panels) and UND data (often used to ascertain presence of microburst asymmetry) in the lower left panel indicated microburst-strength divergence existed in the 18.7 m/s alarm region, whereas the TDWR (lower right) observed only 9 m/s of shear. Viewing angles of this event were more similar between the ASR and UND, so microburst asymmetry was assumed. Similarly, when a microburst was not evident in the ASR data, but was present in the TDWR data because of microburst asymmetry, the ASR-WSP system was penalized with misses. The lack of a microburst-strength signature in the UND velocity field confirmed the asymmetry.

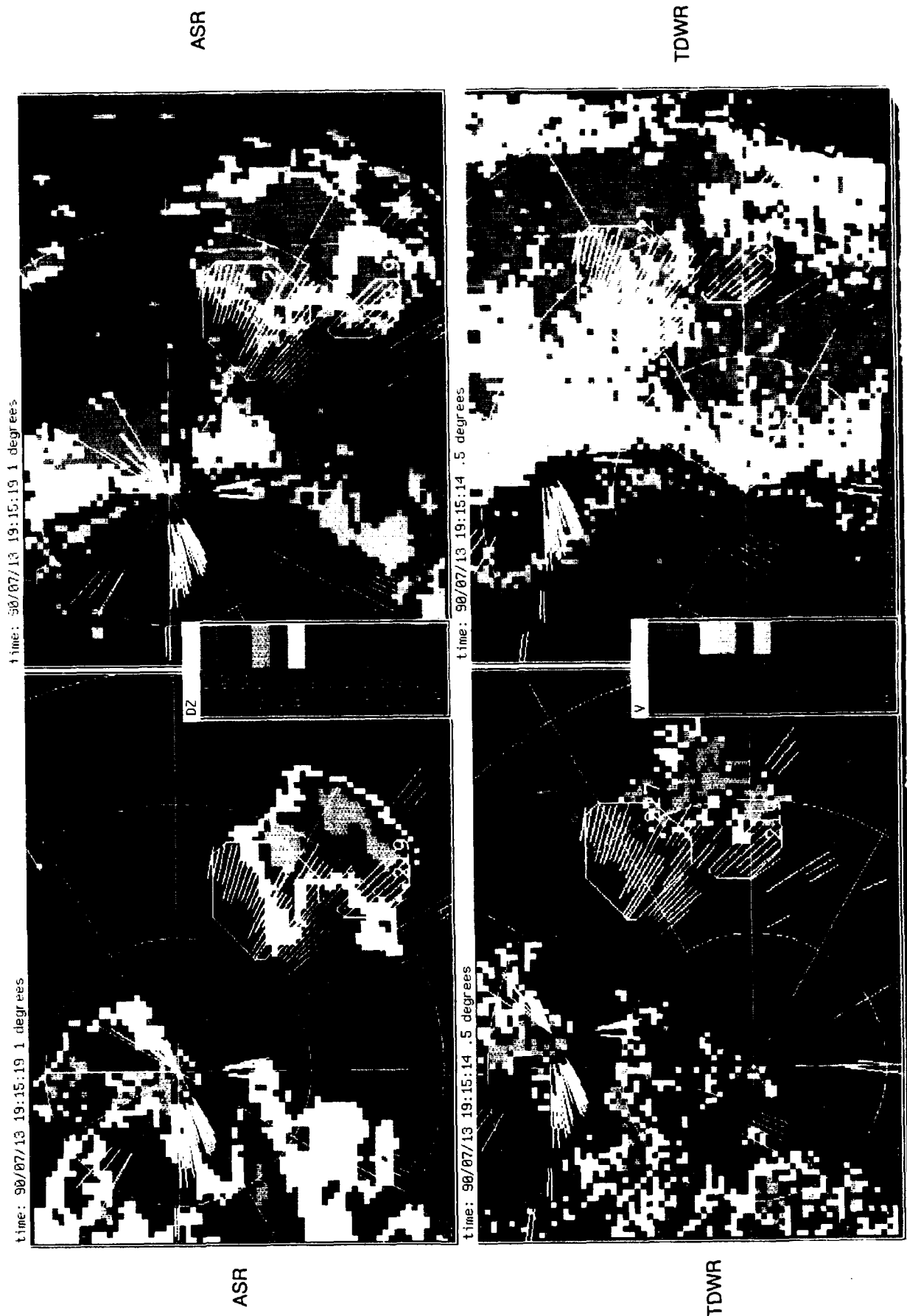
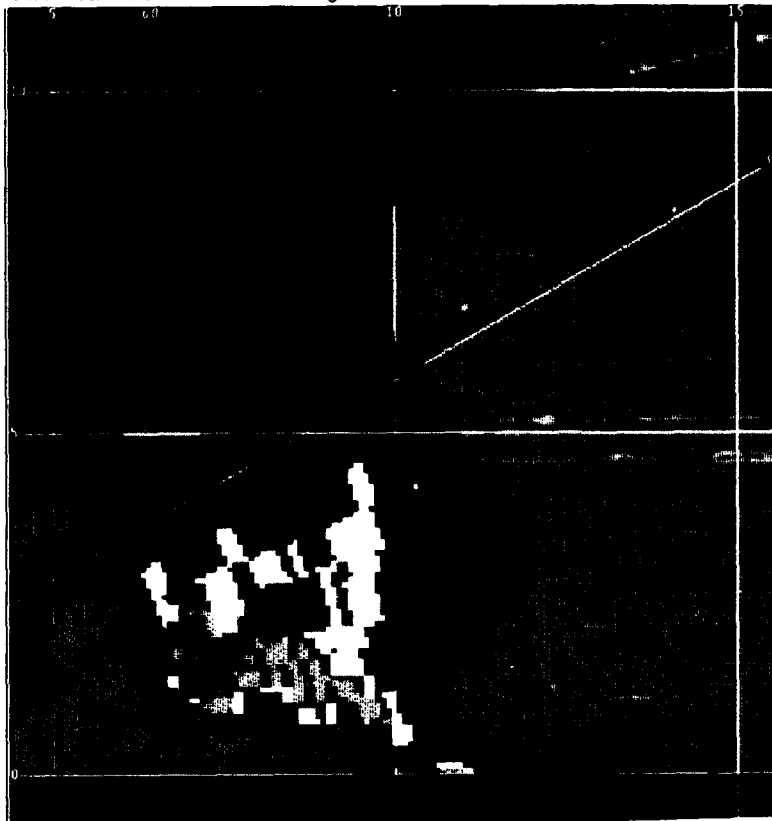


Figure 20. False alarm at 7 km, 120 degrees from ASR (9 km, 60 degrees from TDWR) due to elevated reflectivity core. Region of 6 m/s approaching velocities within the alarm were associated with elevated core (see Figure 21).

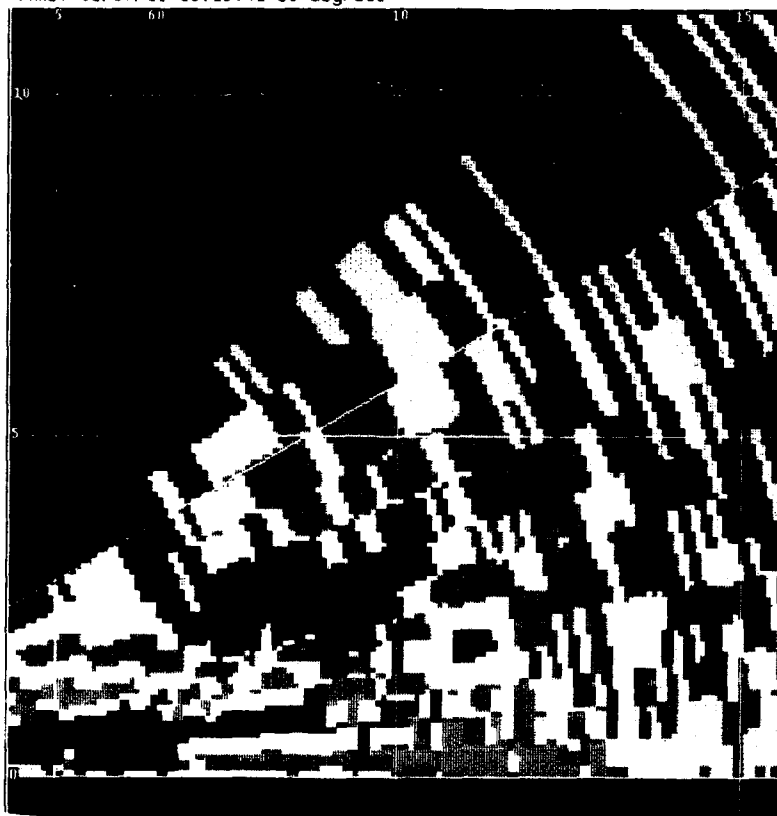
time: 98/07/13 19:13:41 68 degrees



DZ



time: 98/07/13 19:13:41 68 degrees



V



Figure 21. Synthesized RHI scan through location of false alarm in Figure 20. Negative velocities associated with elevated reflectivity core dominate ASR surface velocity estimate because they coincide with strongest signal return.

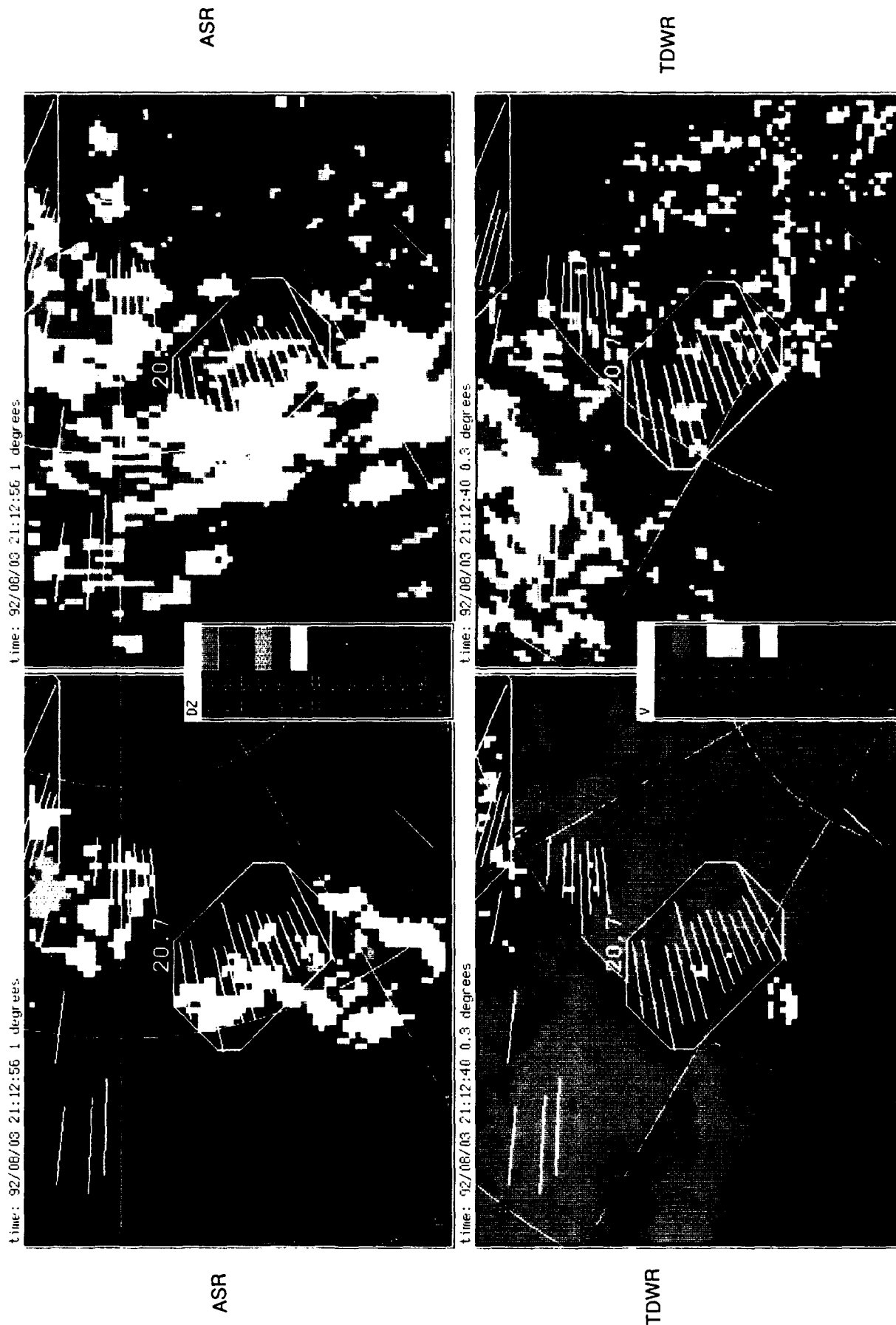


Figure 22. ASR-9 Microburst Detection Algorithm's use of velocity estimates in areas of low signal return caused 20 m/s false alarm. TDWR data (bottom panels) and UND data (not shown) confirmed the lack of microburst-strength divergence in the alarm region.

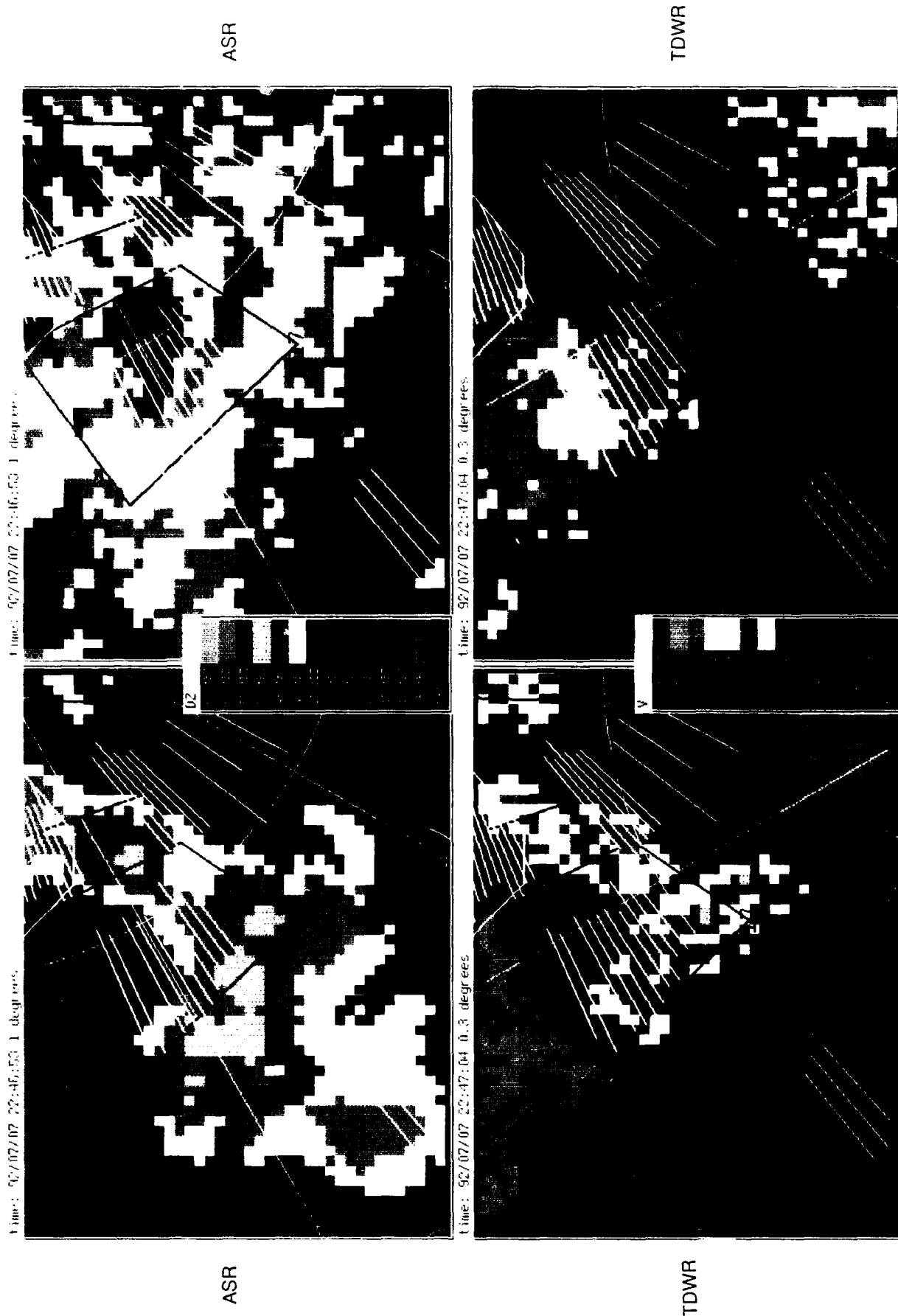


Figure 23. Missed microburst due to microburst algorithm area thresholding. Area of cluster of divergence segments in ASR data (top panels) did not exceed minimum required for event at this range and of this intensity. Nearest TDWR data appears in bottom panels.

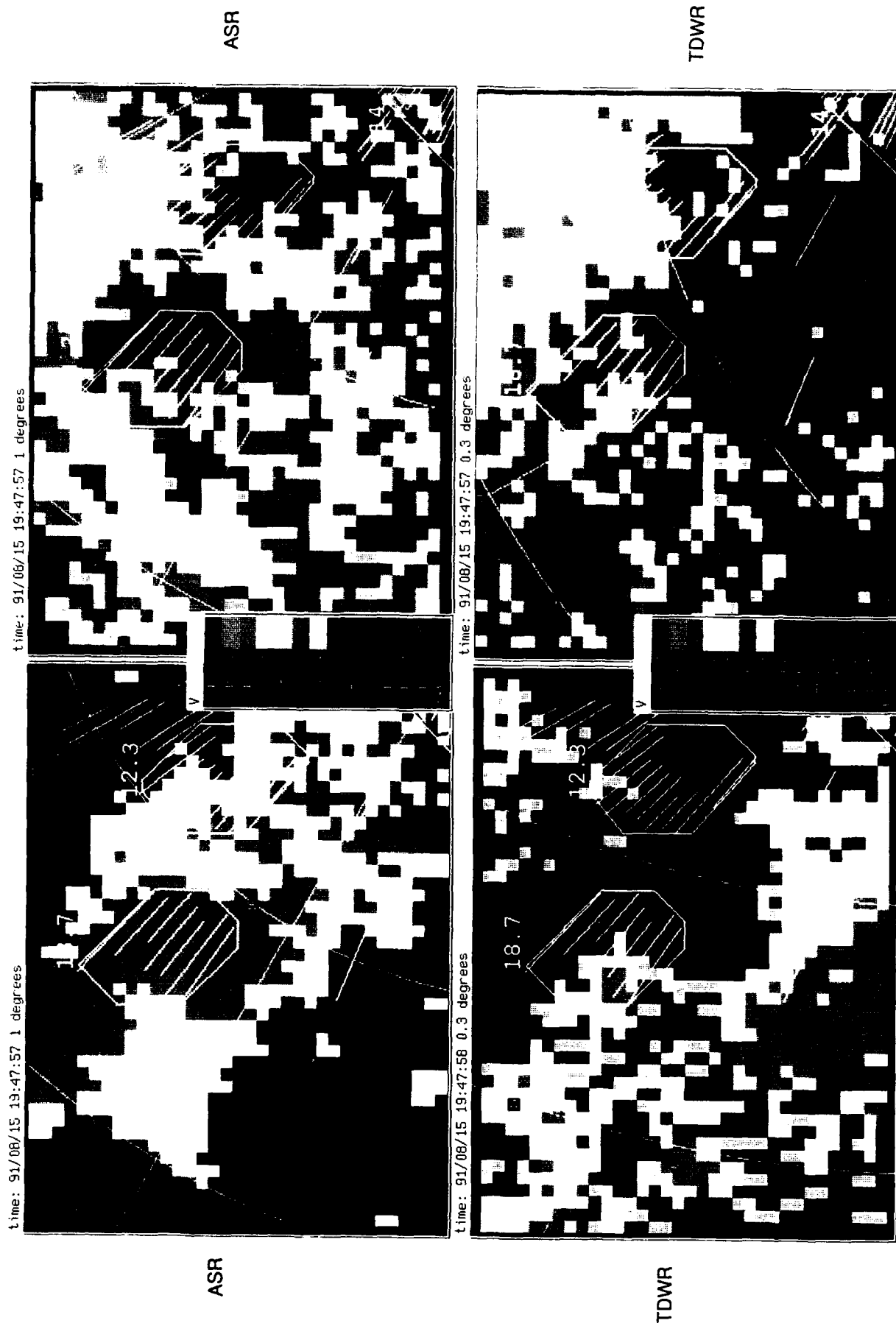


Figure 24. Apparent false alarm by the ASR-WSP system due to microburst asymmetry. UND velocity data at lower left confirms presence of microburst-strength shear at 12 km, 310 degrees azimuth from the ASR (top panels). Only marginal microburst-strength divergence was observed by the TDWR (lower right).

The main types and causes of AMDA failure have been described above. As indicated, many of the observed shortcomings were induced by physical characteristics of the ASR and current signal processing techniques. Improved algorithm performance is expected after enhancements to the latter. Slight modifications to the algorithm itself might also augment detection performance.

6. ONGOING ALGORITHM DEVELOPMENT

There are two separate paths for ongoing ASR-9 microburst algorithm development. The first involves relatively minor changes to the existing version of AMDA to improve its performance using techniques that have become apparent during the past year of data analysis. The second involves alternative algorithm approaches, motivated by recent work on both the ASR-9 Gust Front Algorithm [Delanoy, Troxel, 1993] and the Integrated Terminal Weather System (ITWS) Microburst Detection Algorithm [Campbell, 1992].

6.1 AMDA ENHANCEMENTS

AMDA has been relatively stable since August 1991, but no relatively complex algorithm is ever completely "finished"; AMDA is no exception. As the volume of analyzed data has continued to grow, problem areas have been uncovered, and minor modifications to the algorithm are continually being evaluated as possible solutions. As indicated in the performance evaluation section, noisy velocity estimates in areas of low reflectivity (< 20 dBZ) can pose a problem. The noisy estimates are not usually coherent enough to cause a false alarm on their own, but they can cause a significant error in the velocity estimate for true microbursts or wind shears. The most common result is that an event that is actually only a wind shear alert (< 30 knots) is declared a microburst alert category, contributing to the FAR for the stronger alarms. A modification to the current reflectivity thresholding logic is being evaluated as a solution to this problem. A threshold would be applied to the entire velocity field prior to the segment detection process, thereby eliminating the possibility that valid shear segments contain velocity values from areas of questionable signal quality.

A second problem related to reflectivity thresholding is the performance of AMDA in a dry environment. To date, all ASR-9 microburst data have been collected in wet environments. This will change in 1993 with the relocation of the radar to Albuquerque, New Mexico. To detect dry microbursts that are present during the same period as higher reflectivity storm cells, the current reflectivity thresholding logic will need further modification. Specifically, to avoid the removal of all dry microburst shear segments, the reflectivity threshold parameter will have to be set on a storm cell-by-storm cell basis instead of utilizing a single threshold over the entire scan.

Though the final microburst outputs are being temporally smoothed, the temporal stability of the alarms can sometimes still be a problem. When multiple microbursts are present and in close proximity to one another, the shapes produced by the current algorithm can occasionally change significantly from scan to scan. This is not appropriate output for a rapid update data stream to an ATC environment, and becomes even more of an issue if microburst warnings are updated more rapidly than the 30-second interval used currently during operational demos. A scan-to-scan microburst shape interpolation strategy, as well as improvements to current temporal smoothing logic and shape generation algorithm [Wilson, et. al. 1992], are being studied as solutions to this problem.

6.2 ALTERNATIVE ALGORITHM APPROACHES

When the original design goals of AMDA are reexamined, it becomes apparent that some of them are no longer as important as they were in 1988. Changes in computer hardware and software, as well as in the definition of what constitutes the "danger zone" of a microburst, have occurred since that time, and have prompted a renewed interest in alternative approaches. This section provides a brief history of the development of the current algorithm, and describes some perceived shortcomings of AMDA that could be rectified by replacing the algorithm with one that uses more refined image processing techniques.

6.2.1 AMDA DEVELOPMENT HISTORY

When the TDWR microburst algorithm was first developed, it was decided that the basic goal was to detect the peak approaching and receding velocities, and calculate a shear value (Δv) as the difference between the two peak values. A second design consideration was the decision to run the algorithm on an essentially raw (unsmoothed) velocity field, again in the interest of detecting the absolute peak velocity values. The combination of these two factors made the implementation of a strictly shear field-based algorithm difficult because the small window size required for detection of absolute velocity extrema was also sensitive to noise in the raw velocity field. For this reason, a segment-based point-to-point search algorithm [Merritt, 1987] was developed instead of a conceptually simpler shear-field based algorithm [Noyes, 1990], and while the resulting algorithm is somewhat tricky to tune, it has been very successful in meeting its design goal.

The ASR-9 microburst detection algorithm was not required to mimic the TDWR approach. In fact, the design considerations were slightly different. Due to spatial smoothing, the ASR-9 velocity field was smoother than the corresponding TDWR field, and an initial implementation of a shear field-based algorithm was successful in detecting microbursts of varying sizes [Noyes, 1990]. This algorithm, however, was still incomplete in early 1989, and a requirement existed to have a microburst algorithm running in the WSP that summer. To accomplish this, a simple adaptation of the TDWR algorithm (AMDA) was developed for the WSP. During early 1990 the shear-based algorithm was completed, and although it was conceptually simpler, tests conducted using recorded ASR-9 data indicated it had approximately equivalent performance to AMDA and was more computationally intensive, requiring additional processing power to keep pace with the 12 scan/min antenna rotation rate. Because the performance of the two algorithms was equivalent and AMDA was already running in real time in the WSP, AMDA remained the algorithm of choice for the 1990-1992 time period.

6.2.2 MOTIVATION FOR ALTERNATIVE ALGORITHMS

Although AMDA runs efficiently and has performed well during the operational test periods, there are several arguments for converting the algorithm to a shear field-based approach. The main argument is that the existing segment-based ASR-9 and TDWR algorithms do not necessarily provide an accurate estimate of the windspeed loss an aircraft will experience when passing through a

microburst. In many cases during the operational demonstrations, pilots flying through wind shear events would not encounter the predicted loss value because the current warning supplies only the overall peak-to-peak velocity differential, with no information about the rate of change. For example, the loss value provided to pilots for a 40-knot microburst with a diameter of 4 km is identical to the loss for a 40-knot microburst with only a 1 km diameter, but an aircraft will be affected quite differently in the two cases. Furthermore, two microbursts with identical size and peak-to-peak velocity difference may also be quite different if the shear is spread out fairly evenly in one case but not in the other. A recent study conducted for TDWR compared the issued microburst warnings with the actual performance degradation encountered by a research aircraft flying through over 60 microbursts in Orlando, Florida [Campbell, 1992]. The performance degradation on board the aircraft was measured using a hazard index known as "F-factor" [Bowles, 1990], which takes into account the overall energy balance of the individual aircraft as well as the surrounding environment. To make the ground-based radar warnings compare favorably with the measured F-factor data, it was necessary to compute an equivalent F-factor using a shear field. In light of this result, it would be desirable to have the shear field available to the algorithm, so that any future upgrades to the algorithm outputs could include the shear information.

Recent work in the area of gust front detection has resulted in the new ASR-9 Machine Intelligent Gust Front Algorithm (MIGFA) [Delanoy, Troxel, 1993]. This algorithm has its roots in advanced image processing techniques (also utilizing a shear field) and is a dramatic improvement, both in performance and in ease of modification, over the previous segment-based algorithm. The major challenge when detecting gust fronts with an ASR-9 is the ability to extract gust front thinlines from low SNR radar data. This is similar to the problem of "dry" microburst detection with an ASR-9, and given the success of MIGFA in this regard, it may prove necessary to test this approach for dry microburst detection as well. Since the WSP will already contain one algorithm of this type, this strategy would also make the overall architecture of the WSP more consistent, and therefore easier to produce and maintain.

No major commitment has yet been made to replace AMDA with a more flexible and computationally intensive shear field-based algorithm. Much of the background work has already been performed however, and the effort required to finish the task is certainly not overwhelming. The current generation of processing hardware provides sufficient performance to do the job, and a new "machine-intelligent" shear-based algorithm could be ported to the WSP given sufficient resources.

7. SUMMARY

AMDA evolved from the TDWR microburst detection algorithm and has been optimized for the ASR-9 radar. Like the TDWR algorithm, AMDA detects shear segments, and groups the segments into wind shear alerts and microburst alarms. Unlike the TDWR algorithm, AMDA utilizes a coordinate system shift to process overhead data in a convenient manner, and also makes use of the reflectivity field to help eliminate false alarms caused by precipitation aloft. The algorithm is efficient, currently running in real time on a 5 MIP, 68030-based single board computer with a worst-case CPU usage of approximately 30 percent.

AMDA has been successful during the operational evaluation test periods in Orlando during the past two summers, with an average detection performance of 97 percent and a false-alarm rate not exceeding 10 percent for events stronger than 30 knots and within 8km. AMDA has not yet undergone testing in a dry environment, and changes to the algorithm, specifically in the reflectivity thresholding area, may be necessary to achieve acceptable performance in this case. The move to Albuquerque in 1993 should provide the necessary dry microburst data to evaluate the algorithm in this regard.

Increased understanding of the operational issues associated with microburst detection, and the successful implementation of the Machine Intelligent Gust Front Algorithm have prompted a renewed interest in alternative algorithm approaches. With the advent of faster computer hardware, real-time implementation of these computationally intensive approaches is now becoming more practical, and it is worth evaluating these methods when performing further algorithm development. Potential benefits of a "Machine Intelligent" microburst algorithm include improved performance, particularly in challenging meteorological environments, and greater consistency among the WSP microburst and gust-front algorithms.

REFERENCES

1. R.L. Bowles, "Reducing Windshear Risk Through Airborne Systems Technology," 17th Congress of the International Council of the Aeronautical Sciences, Stockholm, Sweden, September, 9-14, 1990.
2. S.D. Campbell, A. Berke, M. Matthews, "Orlando TDWR Testbed and Airborne Wind Shear Data Comparison Results," Fourth Combined Manufacturers' and Technologists' Conference, September, 1992.
3. R.L. Delanoy, S.W. Troxel, "The Machine Intelligent Gust Front Algorithm," MIT Lincoln Laboratory, Project Report ATC-196, (publication pending) 1993.
4. R.G. Hallowell, "Dual-Doppler Measurements of Microburst Outflow Strength Asymmetry," 26th Conference on Radar Meteorology, May, 1993.
5. M.W. Merritt, "Automatic Detection of Microburst Windshear for Terminal Doppler Weather Radar," Digital Image Processing and Visual Communications Technologies in Meteorology, Cambridge, MA, 26-28 October, 1987.
6. M.W. Merritt, "Microburst Divergence Detection for Terminal Doppler Weather Radar," MIT Lincoln Laboratory, Project Report ATC-181, FAA/NR-91/7, September 1991.
7. T.A. Noyes, "Divergence Detection in Wind Fields Estimated by an Airport Surveillance Radar," MIT Lincoln Laboratory, Project Report ATC-172, FAA/NR-90/2, October 1990.
8. T.A. Noyes, S.W. Troxel, M.E. Weber, O.J. Newell, J.A. Cullen, "The 1990 Airport Surveillance Radar Wind Shear Processor Operational Test at Orlando International Airport," MIT Lincoln Laboratory, Project Report ATC-178, FAA/NR-91/1, July 1991.
9. M.E. Weber, "Ground Clutter Processing for Wind Measurements with Airport Surveillance Radars," MIT Lincoln Laboratory, Project Report ATC-143, FAA/PM-87/21, November 1987.
10. M.E. Weber and W.R. Moser, "A Preliminary Assessment of Thunderstorm Outflow Wind Measurement with Airport Surveillance Radars," MIT Lincoln Laboratory, Project Report ATC-140, FAA/PM-86/38, May 1987.
11. M.E. Weber and T.A. Noyes, "Low-Altitude Wind Shear Detection with Airport Surveillance Radars: Evaluation of 1987 Field Measurements," MIT Lincoln Laboratory, Project Report ATC-159, FAA/PS-88/10, August 1988.
12. M.E. Weber, "Dual-Beam Autocorrelation Based Wind Estimates from Airport Surveillance Radar Signals," MIT Lincoln Laboratory, Project Report, ATC-167, FAA/PS-89/5, June 1989.
13. M.E. Weber, "Airport Surveillance Radar Wind Shear Processor: 1991 Test at Orlando, FL," MIT Lincoln Laboratory, Project Report ATC-189, FAA/NR-92/7, June 1992.
14. F.W. Wilson Jr., R.K. Goodrich, K. Brislawn, "Enclosing Shapes for Single Doppler Radar Features," *Journal of Atmospheric and Oceanic Technology*, Volume 9, No. 2, 97-107, April, 1992.

Appendix A AMDA Parameters

This appendix contains a list of all the adjustable parameters used by AMDA. The current settings are shown in parentheses to the right of each parameter.

Segment Detection Parameters

| | |
|------------------------------|--|
| SEG_MAX_1ST_INC (5.0 m/s) | Maximum velocity differential between first two gates of a segment. |
| SEG_MIN_LENGTH (.96 km) | Minimum length for a segment to be considered valid. |
| SEG_MIN_SHEAR (7.8 m/s) | Minimum velocity differential for a segment to be considered valid. |
| MAX_SUM_DECREASES (5.0 m/s) | Maximum value for <i>sum_decreases</i> . Values exceeding this will cause the segment growing process to terminate. |
| SUM_DECREASES_ADJ (1.0 m/s) | Adjustment value to apply to <i>sum_decreases</i> when a velocity <i>increase</i> is encountered and <i>sum_decreases</i> is non-zero. |
| SEG_MAX_BAD_VALS (2) | Maximum number of bad values allowed in a segment. |
| SEG_MIN_SLOPE (1.8 (m/s)/km) | Minimum slope requirement for segments. Segment regions with slope less than this are trimmed away. |

Segment Temporal Smoothing Parameters

| | |
|-----------------------|---|
| SEG_AGE_MIN (3 scans) | Minimum value for the <i>seg_age</i> variable before a segment can be inserted into a scan where it is missing. |
| SEG_AGE_MAX (7 scans) | Maximum value allowed for the <i>seg_age</i> variable. The formula (SEG_AGE_MAX - SEG_AGE_MIN) represents the maximum number of segment insertions that can be done after a segment disappears. |

Segment Association Parameters

| | |
|---------------------------------|---|
| SEG_OVERLAP_PERCENTAGE (50%) | Percentage of the segment to use in the overlap test. In this case, only the middle 50% of the segment is used for overlap testing. |
| CLU_MIN_SEGS (4) | Minimum number of segments in a cluster. |
| CLU_MIN_AZ_WINDOW (3) | Minimum azimuth window to use during segment association. The azimuth window varies with range, and this group of 4 parameters defines the endpoints of a linear azimuth window vs. range equation. |
| CLU_MIN_AZ_WINDOW_RANGE(10.0km) | Range at which to use the minimum azimuth window. |
| CLU_MAX_AZ_WINDOW (11) | Maximum azimuth window to use during segment association. |

CLU_MAX_AZ_WINDOW_RANGE(0.0km) Range at which to use the maximum azimuth window.

Reflectivity Thresholding Parameters

REFL_THRESH_CORE_DBZ (40.0 dBZ) Core reflectivity used for reflectivity threshold.

REFL_THRESH_SEG_LEN_IN_CORE(50%) Percentage of segment length that must lie within a region of core reflectivity in order for the segment to be considered valid.

REFL_THRESH_DIST (0.5 km) Distance used in the last stage of the reflectivity thresholding process. Segments within this distance from a segment that has passed the reflectivity test are also considered valid.

Segment Density Thresholding Parameters

SEG_DENSITY_THRESH (0.5) Segment density thresholding parameter. Cluster segments in regions where the segment density is below this fraction are discarded.

Area Thresholding Parameters

CLU_AREA_MIN (0.5 km²) Baseline value of area threshold.

CLU_AREA_RANGE_MIN (2.0 km²) Minimum range for area threshold range correction.

CLU_AREA_RANGE_MAX (16.0 km²) Maximum range for area threshold range correction.

CLU_AREA_RANGE_SLOPE (0.1 km²/km) Rate of change of area threshold with respect to range.

CLU_AREA_SHEAR_A (30) A Coefficient for area threshold shear correction.

CLU_AREA_SHEAR_B (2.5) B Coefficient for area threshold shear correction.

CLU_AREA_SHEAR_C (-1.0) C Coefficient for area threshold shear correction.

Cluster Temporal Smoothing Parameters

CLU_MIN_AGE (3 scans) Minimum cluster age. Younger clusters are not output as microburst events.

CLU_COAST_SCANS (12 scans) Number of scans to coast a cluster if it is dropped.